An Optimal Zero-Sequence Component Injection Method With Reduced Low-Frequency Voltage and Current Ripples for Improved Three-Phase Three-Level Multiport Converter

Nengmou Xu, *Student Member, IEEE*, Guohua Zhou, *Senior Member, IEEE*, Yingjie He, Qingxin Tian, *Member, IEEE*, Qiang Bi, and Wenjun Zeng

***Abstract*—It is a desirable solution to integrate photovoltaic (PV) and energy storage (ES) into ac grid using a multiport converter due to its high efficiency and reliability. In this article, an improved three-phase three-level multi-port converter (TPTL-MPC) is presented for the PV, ES, and grid-connected hybrid systems, which can effectively reduce power conversion stage, thereby further enhancing overall system efficiency. Moreover, an optimal zero-sequence component (ZSC) injection method is proposed to reduce inductor current ripple under active power, reactive power, and different operational modes and dc port voltage. Meanwhile, the proposed optimal ZSC injection method can also reduce low-frequency voltage and current ripples of the PV port and ES port, which is beneficial for reducing the filter capacitors at the ports. To accommodate the voltage variation of PV and ES, dc voltage ratio-based sinusoidal pulsewidth modulation and its digital implementation for improved TPTL-MPC are proposed. The smooth switching between the various operational modes is also realized by the control strategy. Finally, the experimental results have been provided to confirm effectiveness and feasibility of the improved TPTL-MPC based on the proposed optimal ZSC injection method.**

***Index Terms*—Grid-connected system, improved three-phase three-level multiport converter (TPTL-MPC), photovoltaic (PV) and energy storage (ES), zero-sequence component (ZSC) injection.**

I. Introduction

THE integration of energy storage (ES) systems, such as batteries, with photovoltaic (PV) is essential to ensure stable, reliable, and smooth power supply, due to the unpredictability and variation of PV [1], [2], [3]. Combining the PV energy with the ES devices for grid-connected transmission is one of the most widely applied applications in hybrid dc/dc/ac systems [4], [5], [6]. The ES devices can absorb the excess energy released by the PV when the solar power is abundant, and provide energy to the grid when the solar power is insufficient. Consequently, the converters connecting these ports are important and primarily responsible for achieving maximum power point tracking (MPPT) or constant voltage control of the PV port, the bidirectional power flow control of the ES port and grid port [7], [8], [9].

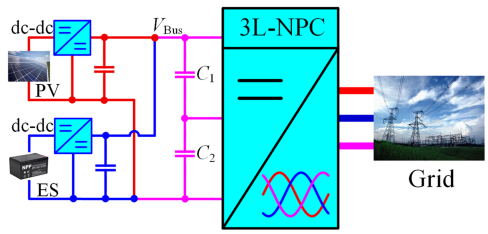

Fig. 1. Conventional two-stage solution based on three-phase 3L-NPC.

In the conventional two-stage solution for PV and ES and grid-connected applications, each dc or ac port is served by an individual converter, and these converters is interconnected through a common dc-bus or ac-bus [10], [11]. The conventional two-stage solution based on dc-bus architecture and three-level neutral-point-clamped (3L-NPC) structure is shown in Fig. 1. Obviously, the advantage of this configuration is the independent control of each port, with low coupling among ports [12], [13]. The primary drawback of a two-stage solution lies in the necessity to process all power twice, resulting in reduced overall efficiency and increased costs due to excessive requirements for power converters [14], [15], [16]. To reduce the number of converters and the stages of energy conversion, and enhance system efficiency in a conventional two-stage solution, an effective solution is to implement a system architecture based on three-phase dc–dc–ac multiport converter (MPC) [17]. This configuration integrates multiple power ports, specifically including the PV port, ES port, and three-phase grid port. Neira et al. [18] propose three-port full-bridge bidirectional converter to interconnect two

Received 12 August 2025; revised 20 October 2025; accepted 21 December 2025. Date of publication 24 December 2025; date of current version 20 March 2026. This work was supported by the National Natural Science Foundation of China under Grant 62271417, Grant 62301482, and Grant 62571353. Recommended for publication by Associate Editor Y. Li. *(Corresponding authors: Guohua Zhou; Qingxin Tian.)*

Nengmou Xu, Guohua Zhou, Yingjie He, Qingxin Tian, and Wenjun Zeng are with the School of Electrical Engineering, Southwest Jiaotong University, Chengdu 611756, China (e-mail: nengmouxu@my.swjtu.edu.cn; eeghzhou@swjtu.edu.cn; hh_123@my.swjtu.edu.cn; qxtian@swjtu.edu.cn; zengwenjun@my.swjtu.edu.cn).

Qiang Bi is with the State Key Laboratory of Power System Operation and Control, Department of Electrical Engineering, Tsinghua University, Beijing 100084, China (e-mail: bq_pece@163.com).

Color versions of one or more figures in this article are available at https://doi.org/10.1109/TPEL.2025.3647968.

Digital Object Identifier 10.1109/TPEL.2025.3647968

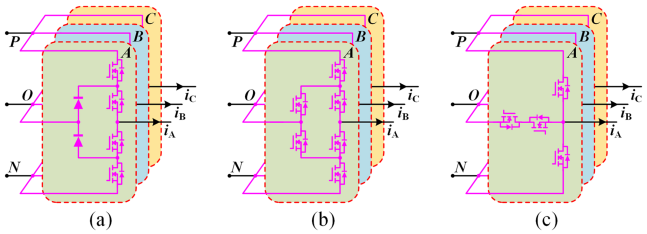

Fig. 2. Basic topologies of the three-phase 3L-NPC for multiport converter. (a) Diode-NPC. (b) Active-NPC. (c) T-type NPC.

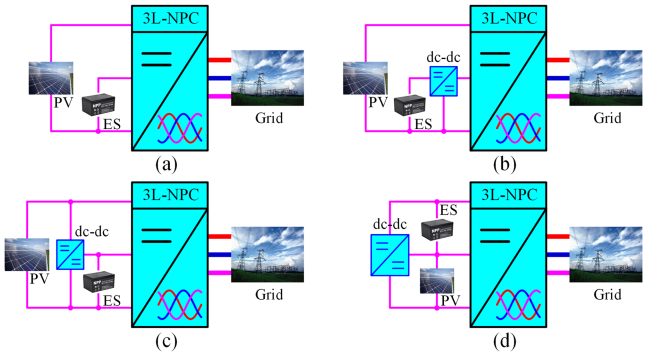

Fig. 3. Several structures of MPC based on three-phase 3L-NPC. (a) Structure I. (b) Structure II. (c) Structure III. (d) Improved structure.

dc ports with a single-phase or three-phase ac port. The topology employs fewer components to achieve integration of the PV, ES and three-phase grid port, but it is characterized by relatively large inductor current ripples and complex control method.

Furthermore, the MPCs based on three-phase 3L-NPC topologies are currently recognized as one of the most significant solutions. As shown in Fig. 2, the basic topologies of the three-phase 3L-NPC suitable for MPC include diode-NPC, active-NPC and T-type NPC, which have three dc ports and a three-phase ac port. To utilize this characteristic, several MPCs based on three-phase 3L-NPC and their advanced modulation and control methods are investigated in existing literatures [19], [20], [21], [22], [23]. These structures of MPCs based on three-phase 3L-NPC are classified into three types, [19], [22], [23], as shown in Fig. 3(a)–(c), respectively. The existing three structures of MPC based on three-phase 3L-NPC can significantly reduce the count of component, compared to the conventional two-stage solution (as shown in Fig. 1). Wang et al. [19] propose a dual-dc-port dc–ac converter with virtual space vector pulse width modulation based flexible power control for PV-battery hybrid systems, in which the bus is connected to the PV, and the low-voltage port is connected to the battery. And the structure I of [19] is shown in Fig. 3(a). This topology fully utilizes the advantages of three-phase 3L-NPC topologies. Several excellent modified modulations and advanced control strategies are proposed for the structures I, such as [20], [21], etc.

Moreover, the structure II is based on structure I, adding dc–dc unit among the battery and low-voltage port is shown in Fig. 3(b) [22], with reducing common-mode voltage. And it enables more flexible adjustment of the low-level voltage. However, it exhibits the high degree of coupling, complex modulation and control strategy, and limited power control range. In addition, there are relatively large voltage and current ripples in the PV and battery ports, and the solution is usually to parallel capacitors at the dc ports. In order to solve above problem, a multiport dc–ac converter with differential power processing dc–dc converter and its flexible power control is proposed in [23]. Based on the structure in Fig. 3(a), a bidirectional buck-boost unit in Fig. 3(c) is added to realize the differential power processing in [23]. However, this topology still presents the challenge of the grid frequency (low-frequency) voltage and current ripples, and it also needs higher dc voltage of the PV or battery. In [24], [25], and [26], the higher bus voltage is supplied with the method of connecting two dc port in series, which can reduce the dc voltage requirements of the PV or battery. Moreover, there are different voltage and current ripples under different dc port voltage and modulation, which is not conducive to parameter designs of the MPCs. It also affects voltage and current ripples of the PV and battery ports and smooth switching of several operational states. The large voltage and current ripples are detrimental to the service life of PV and battery, and can even lead to system instability and other hazards [27].

All above the three structures in Fig. 3(a)–(c) require a high-voltage dc port and a low-voltage dc port. For example, the PV voltage should be more than twice the peak phase voltage of grid. And the PV voltage should be greater than the battery voltage. In order to solve above problem, the improved structure is proposed, as shown in Fig. 3(d). Certainly, compared with structure I in Fig. 3(a), an additional dc–dc unit has been added in the improved structure, resulting in a slight increase in the number of components. However, the improved structure can reduce the voltage requirements of the exiting MPC. It only requires that the sum of the battery voltage and the PV voltage is greater than the value of the phase peak voltage. Obviously, the improved structure exhibits relatively relaxed port voltage constraints.

Inspired by state-of-the-art solutions in the aforementioned literatures, the improved structure of three-phase three-level MPC (TPTL-MPC) based on 3L-NPC is presented, as shown in Fig. 3(d). Moreover, to reduce low-frequency voltage and current ripples of the PV and battery, the optimal zero-sequence component (ZSC) injection method is proposed. The major contributions of improved TPTL-MPC and proposed optimal ZSC injection method are summarized as follows.

1) The improved TPTL-MPC based on bidirectional dc-dc unit and three-phase 3L-NPC unit is presented, which can reduce power conversion stage and voltage requirements of the PV and battery ports. The dc voltage ratio-based sinusoidal pulsewidth modulation (DVR-SPWM) and the easy digital implementation method are also proposed.
2) The optimal ZSC injection method is proposed, which eliminates inductor current low-frequency ripple under active power, reactive power, different operational modes and dc port voltage. It can also effectively reduce voltage and current ripples of the PV and battery, which can reduce input capacitor and enhance reliability of dc ports.
3) Combining improved TPTL-MPC, the proposed DVR-SPWM and optimal ZSC injection method, the relaxed

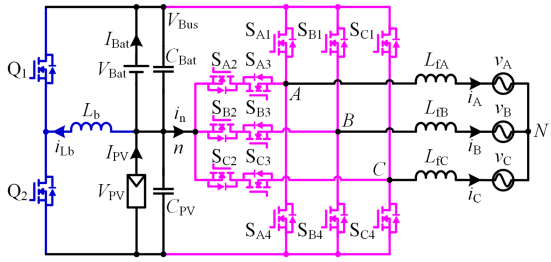

Fig. 4. Topology of improved TPTL-MPC.

port voltage constraints, the lower degree of coupling, wide power range, lower total harmonic distortion (THD) of grid current, and the higher efficiency are also achieved.

4) The MPPT of PV and bidirectional power flow for ES port and three-phase grid port can be realized, and smooth switching between the various operational modes is also realized by the control strategy of improved TPTL-MPC.

The rest of this article is organized as follows. In Section II, the operational principle and DVR-SPWM of improved TPTL-MPC are analyzed in detail. Section III introduces the inductor current ripple analysis, investigation into impact of ZSC injection method on the inductor current low-frequency ripple, the proposed optimal ZSC injection method, and control strategy. Comparison results and analysis for other TPTL-MPCs and ZSC injection methods are given in Section IV. The effectiveness and feasibility of improved TPTL-MPC and its DVR-SPWM, the proposed optimal ZSC injection method, and control strategy are validated by the experimental results in Section V. Finally, Section VI concludes this article.

II. Operational Principle and DVR-SPWM of the Improved TPTL-MPC

A. Operational Modes and Principles of Improved TPTL-MPC

The topology of improved TPTL-MPC based on a bidirectional buck-boost unit and a three-level T-type NPC unit is presented for the PV, ES, and grid hybrid systems, as shown in Fig. 4. The two low-voltage ports of three-level T-type NPC unit are connected to the PV and battery, respectively. The dc bus voltage is provided by the PV port and the battery port in series. And the two dc ports are connected through a bidirectional buck-boost unit, which can regulate the power between two dc ports.

The improved TPTL-MPC is based on an improved structure in Fig. 3(d). Compared with the conventional two-stage solution in Fig. 1, the improved TPTL-MPC reduces one dc–dc converter, a feature shared with structure II and structure III in Fig. 3, thereby achieving a favorable balance between a relatively low device count and high degree of control flexibility. And the improved TPTL-MPC can also reduce the voltage requirements in the PV and battery port. Furthermore, the T-type three-level NPC (twelve switches) employs fewer semiconductor devices than the active-NPC (eighteen switches) and the diode-NPC (twelve switches, six diodes). Of course, the active-NPC and the diode-NPC have advantages in reducing voltage stress for the higher voltage scenario.

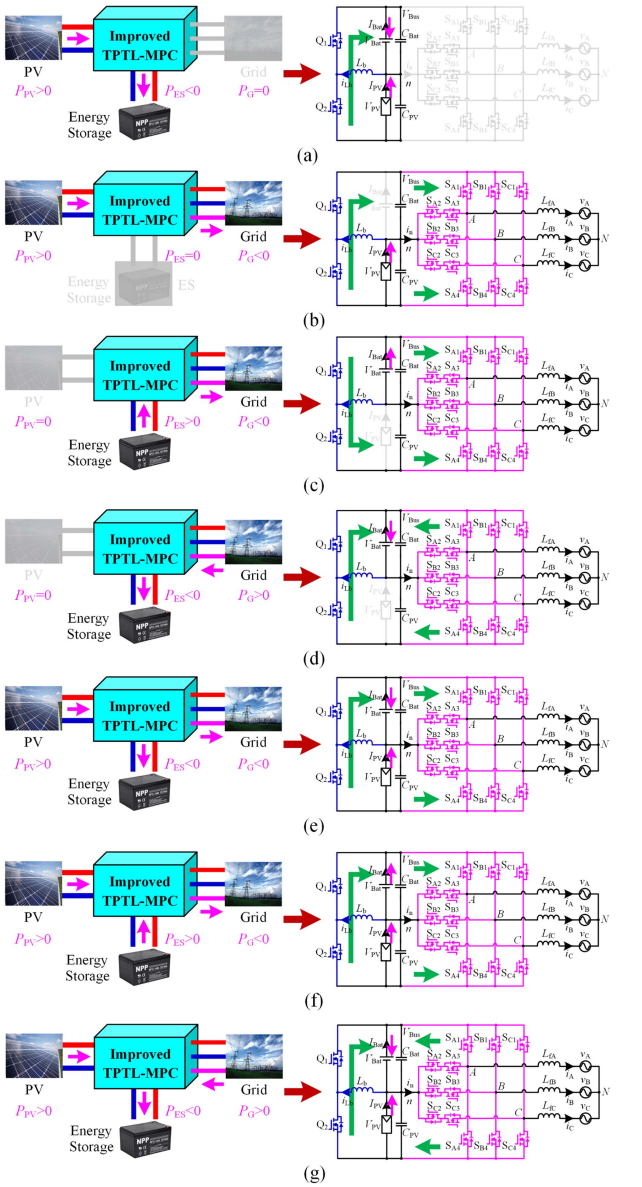

Fig. 5. Operational modes and circuit states of improved TPTL-MPC during various modes. (a) PV to battery mode. (b) PV to grid mode. (c) Battery to grid mode. (d) Grid to battery mode. (e) PV to battery and grid mode. (f) PV and battery to grid mode. (g) PV and grid to battery mode.

The improved TPTL-MPC experiences a variety of operational modes based on the statuses of the PV, ES, and grid in practical applications. And the operational modes and circuit states of improved TPTL-MPC during various modes are illustrated in Fig. 5, encompassing seven distinct scenarios where any of these ports may either disconnect or experience changes in output power. For the convenience of expression, the power of PV, ES and grid are respectively defined as P_{PV}, P_{ES}, and P_{G}. The relationship between them can be given as

$$P_{\mathrm{PV}} + P_{\mathrm{ES}} + P_{\mathrm{G}} = 0 \tag{1}$$

where the positive power of these ports indicates that energy flows from the ports to the improved TPTL-MPC, and the negative power indicates that the energy flows from the improved TPTL-MPC back to the ports. Moreover, the P_{PV} is greater than or equal to zero, while the power capacity of the ES and grid is variable. As illustrated in Fig. 5, the operational modes and circuit states of improved TPTL-MPC during the various modes are analyzed as follows.

1) *PV to battery mode:* As shown in Fig. 5(a), the grid and T-type NPC unit is idle. The energy of PV is transmitted to the battery through the bidirectional buck-boost unit, and MPPT of PV is realized.
2) *PV to grid mode:* As shown in Fig. 5(b), the battery is idle. The MPPT of PV is realized by the bidirectional buck-boost unit. Moreover, the bus voltage is controlled constant, and the grid-connected is achieved by three-level T-type NPC unit and control strategy.
3) *Battery to grid mode:* As shown in Fig. 5(c), the PV is idle. And the bus voltage is controlled constant by the bidirectional buck-boost unit. Meanwhile, grid-connected control is achieved through a three-level T-type NPC unit. The battery supplies power to the grid, with the battery in discharge state and the grid in inverter state.
4) *Grid to battery mode:* As shown in Fig. 5(d), the PV is idle. And the bus voltage is controlled as a constant by the bidirectional buck-boost unit. Meanwhile, the grid-connected control is achieved through a three-level T-type NPC unit. The grid supplies power to the battery, with the battery in charge state and the grid in rectifier state.
5) *PV to battery and grid mode:* As shown in Fig. 5(e), the PV, battery, and grid are all available. The PV power is sufficient, and the energy from PV is transmitted to grid through a three-level T-type NPC unit, while the residual energy of PV is transmitted to the battery through the bidirectional buck-boost unit. The MPPT of PV and the grid-connected control are also achieved by a bidirectional buck-boost unit and three-level T-type NPC unit.
6) *PV and battery to grid mode:* As shown in Fig. 5(f), the PV, battery and grid are all available. The PV power is insufficient, and the energy from PV and battery is transmitted to grid. The MPPT of PV and the grid-connected control are also achieved by bidirectional buck-boost unit and three-level T-type NPC unit.
7) *PV and grid to battery mode:* As shown in Fig. 5(g), the PV, battery, and grid are all available. This is a special case in which the PV power and the grid power are coordinated to address situations involving battery energy shortages or excessive energy supply from the power grid.

It should be noted that the purple arrow and the green arrow in operational modes and circuit states of Fig. 5 indicate the direction of power flow.

B. Proposed DVR-SPWM of Improved TPTL-MPC

According to the above-mentioned analysis, there exists unbalance voltages for midpoint n. The reason is that the battery voltage V_{Bat} is not necessarily equal to PV voltage V_{PV}. In order

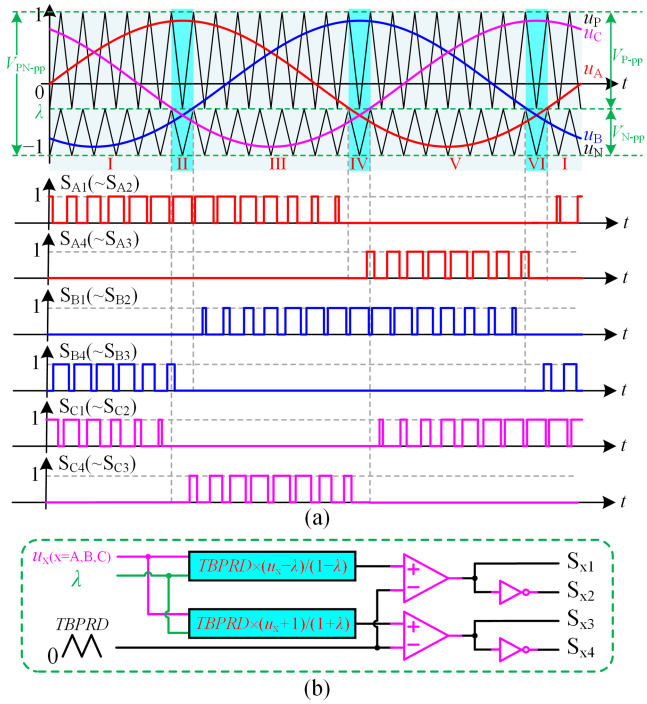

Fig. 6. (a) Waveform of proposed DVR-SPWM for the improved TPTL-MPC. (b) Digital implementation diagram.

to solve the problem, the DVR-SPWM is proposed, which enables timely adjustment of triangular carriers' amplitudes based on actual values of V_{PV} and V_{Bat}. To facilitate the theoretical analysis, assuming $V_{\mathrm{G\text{-}RMS}}$ and V_{Gpk} are the root-mean-square (RMS) value and peak amplitude of the grid, and the angular frequency of the grid $\omega = 2\pi f_{\mathrm{o}}$, where f_{o} is grid frequency. For the three-phase inverter with the DVR-SPWM, the relationship between the V_{Gpk} and the dc bus voltage V_{Bus} is obtained as

$$V_{\mathrm{Gpk}} = \frac{1}{2} M V_{\mathrm{Bus}} \tag{2}$$

where the M is modulation index, and the V_{Bus} is equal to the sum of PV voltage and battery voltage. Therefore, the modulation index M and is calculated as follows:

$$M = \frac{2V_{\mathrm{Gpk}}}{V_{\mathrm{PV}} + V_{\mathrm{Bat}}}. \tag{3}$$

The key waveform of the proposed DVR-SPWM for improved TPTL-MPC is shown in Fig. 6(a). The triangular waves u_P and u_N are carrier of switches $S_{x1}(\sim S_{x2})$-$S_{x4}(\sim S_{x3})$ for three-phase three-level T-type NPC unit, where $x = A, B, C$. And the amplitudes of triangular carriers are adjusted timely based on the port voltage coefficient λ, according to Fig. 6(a). The coefficient λ of the proposed TPTL-MPC is theoretically analyzed as follows. When the battery voltage is equal to PV voltage, DVR-SPWM is equivalent to traditional carrier modulation, and peak-to-peak value $V_{\mathrm{P\text{-}pp}}$ of the upper triangular carrier u_P is equal to peak-to-peak value $V_{N\text{-}\mathrm{pp}}$ of the upper triangular carrier u_N. When the battery voltage is less than the PV voltage, the $V_{P\text{-}\mathrm{pp}}$ is less than $V_{N\text{-}\mathrm{pp}}$. Similarly, the $V_{P\text{-}\mathrm{pp}}$ is greater than $V_{N\text{-}\mathrm{pp}}$, when the battery voltage is greater than the PV voltage. It

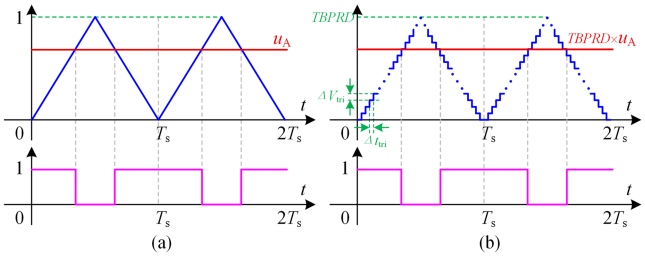

Fig. 7. Waveforms of triangular carrier and modulated wave in (a) theoretical analysis and (b) digital controller.

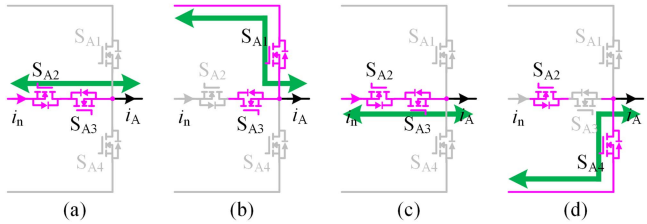

Fig. 8. Equivalent circuits of A-phase in different switching states. (a) $u_A \geq \lambda$, state I. (b) $u_A \geq \lambda$, state II. (c) $u_A < \lambda$, state I. (d) $u_A < \lambda$, state II.

is worth noting that the sum of the peak-to-peak values $V_{\text{PN-pp}}$ of the two triangular waves, as well as the $V_{P\text{-pp}}$ and $V_{N\text{-pp}}$ correspond to the V_{Bus}, V_{Bat}, and V_{PV}, respectively. According to the proportional relationship, the relationship between the $V_{P\text{-pp}}$, $V_{N\text{-pp}}$, and $V_{\text{PN-pp}}$ can be expressed as follows:

$$V_{P-\text{pp}} : V_{N-\text{pp}} : V_{\text{PN}-\text{pp}} = V_{\text{Bat}} : V_{\text{PV}} : V_{\text{Bus}}. \tag{4}$$

In theoretical analysis, the maximum and minimum values of the triangular waves are typically set to 1 and -1 (normalization method), respectively. Therefore, $V_{\text{PN-pp}}$ is equal to 2 in Fig. 6. And the coefficient λ can be calculated

$$\begin{aligned} &V_{P-\text{pp}} : V_{N-\text{pp}} : V_{\text{PN}-\text{pp}} = \frac{2V_{\text{Bat}}}{V_{\text{Bus}}} : \frac{2V_{\text{PV}}}{V_{\text{Bus}}} : 2 \\ &\Rightarrow \lambda = 1 - \frac{2V_{\text{Bat}}}{V_{\text{Bus}}} = -1 + \frac{2V_{\text{PV}}}{V_{\text{Bus}}} \Rightarrow \lambda = \frac{V_{\text{PV}} - V_{\text{Bat}}}{V_{\text{PV}} + V_{\text{Bat}}}. \end{aligned} \tag{5}$$

According to (5) and Fig. 6, the amplitudes of the two triangular waves change in real time as the PV and battery voltages change. This is not favorable for digital controllers. In order to efficiently implement DVR-SPWM in a digital controller, a fixed-amplitude triangular wave is utilized as the carrier signal, while the sinusoidal wave is processed to obtain the modulated signals. Subsequently, both the carrier and modulated signals are fed into a comparator for easy generation of switch gate signals. The digital implementation diagram of DVR-SPWM is illustrated in Fig. 6(b), where the *TBPRD* represents the time-base period register of the digital controller, indicating the amplitude of triangular waveform.

Moreover, in theoretical analysis, the amplitude of triangular carrier is typically normalized to 1, with ranging from 0 to 1, corresponding to the duty cycle of switching signal, as illustrated in Fig. 7(a). However, in digital controller, the triangular carrier does not exhibit ideal continuous characteristic (discretization), as shown in Fig. 7(b). And the step size Δt_{CLK} of the triangular carrier is fixed and determined by the system clock frequency of the digital controller. For each step Δt_{CLK} change in the horizontal coordinate (time), the value of the triangular carrier increases or decreases by 1 ($\Delta V_{\text{tri}} = 1$ or -1). The system clock frequency is f_{CLK} (corresponding to minimum time step $\Delta t_{\text{CLK}} = 1/f_{\text{CLK}}$), and the switching frequency is f_s ($T_s = 1/f_s$). Therefore, the *TBPRD* of the digital controller can be calculated as

$$TBPRD = \frac{1}{2} \times \frac{T_s}{\Delta t_{\text{CLK}}} - 1 = \frac{f_{\text{CLK}}}{2f_s} - 1. \tag{6}$$

It should be noted that the value of triangular carrier ranges from 0 to *TBPRD* in digital controller. Consequently, the -1 term is included in (6). Furthermore, as shown in Fig. 7, the amplitude of triangular carrier is scaled from 1 to *TBPRD*. And modulated wave should also be multiplied by *TBPRD*.

III. Proposed Optimal ZSC Injection Method and Control Strategy

A. Midpoint Current Analysis of Improved TPTL-MPC

For purpose of analysis, assuming the displacement angle between grid voltage and current is φ, and the peak amplitude of grid current is I_{Gpk}. Therefore, initial sinusoidal modulated signals u_A, u_B, u_C, the three-phase grid current i_A, i_B, i_C and grid voltage v_A, v_B, v_C are mathematically described as follows:

$$\begin{cases} u_A = M\sin(\omega t) \\ u_B = M\sin(\omega t - 2\pi/3) \\ u_C = M\sin(\omega t + 2\pi/3) \end{cases} \tag{7}$$

$$\begin{cases} v_A = V_{\text{Gpk}}\sin(\omega t) \\ v_B = V_{\text{Gpk}}\sin(\omega t - 2\pi/3) \\ v_C = V_{\text{Gpk}}\sin(\omega t + 2\pi/3) \end{cases}$$

$$\begin{cases} i_A = I_{\text{Gpk}}\sin(\omega t + \varphi) \\ i_B = I_{\text{Gpk}}\sin(\omega t - 2\pi/3 + \varphi) \\ i_C = I_{\text{Gpk}}\sin(\omega t + 2\pi/3 + \varphi) \end{cases}. \tag{8}$$

Similar to analytical approach employed for conventional T-type NPC inverters, the key distinction lies in the fact that voltages of two low-voltage ports are not necessarily equal. Assuming the midpoint current is i_n, as shown in Fig. 4. The equivalent circuits of A-phase in different switching states are illustrated in Fig. 8, and the green arrow denotes the probable direction of grid current flow. According to the relationship between u_A and λ, there are two cases, each of which has two states. However, the equivalent circuits depicted in Fig. 8(a) and (c) are identical. Consequently, the equivalent circuits of A-phase in different switching states include three types. Obviously, when the switches S_{x2} and S_{x3} of the improved TPTL-MPC are all turned on, the three-phase grid currents i_A, i_B, i_C flow through the midpoint n. Combined with Figs. 6 and 8, the d_x ($x = A$, B, C) are defined as the duty cycle at which both S_{x2} and S_{x3} are turned ON simultaneously. And the d_x can be determined through the mathematical calculations. The grid current can be approximated as constant value during a switching cycle. And the i_n and d_x of improved TPTL-MPC can be theoretically

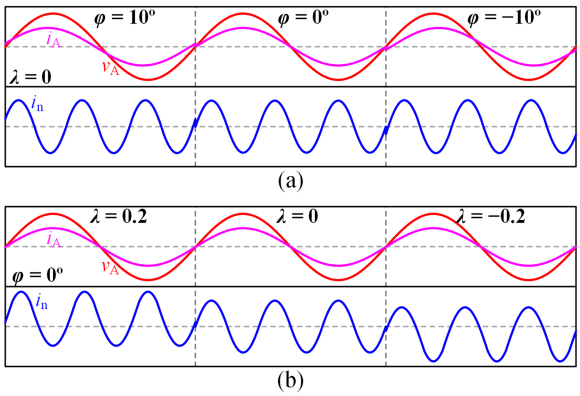

Fig. 9. Low-frequency ripples of midpoint current $i_{\rm n}$ at different λ and φ. (a) $\varphi = 10°, 0, -10°$ when $\lambda = 0$. (b) $\lambda = 0.2, 0, -0.2$ when $\varphi = 0$.

expressed as follows:

$$i_n = \sum_{x=A,B,C} d_x i_x, d_x = \begin{cases} \frac{1-u_x}{1-\lambda}, u_x \geq \lambda \\ \frac{1+u_x}{1+\lambda}, u_x < \lambda \end{cases}. \tag{9}$$

It can be seen from the above-mentioned equations that the midpoint current i_n is only related to three-phase sinusoidal modulated signals u_A, u_B, u_C, three-phase grid currents i_A, i_B, i_C, and coefficient λ. In order to display characteristics of i_n, Fig. 9 shows low-frequency ripples of midpoint current i_n at different λ and φ. The results indicate that the φ influences the phase of i_n when $\lambda = 0$ (indicating midpoint voltage balance), but does not affect its amplitude. On the other hand, the imbalance of midpoint voltage can cause dc bias in i_n. The primary reasons are that when the $V_{\rm PV}$ exceeds $V_{\rm Bat}$ (λ>0), the greater current flows from the midpoint *n* to grid. Conversely, combined with the analysis in Figs. 6 and 8, when the $V_{\rm Bat}$ surpasses $V_{\rm PV}$ (λ<0), the greater current flows from the grid to midpoint *n*.

As illustrated from (9), the midpoint current i_n can be further affected by altering sinusoidal modulated signals when $V_{\rm PV}$, $V_{\rm Bat}$ and grid currents have been determined. This is also fundamental principle of ZSC injection method based on proposed DVR-SPWM. Assuming ZSC is u_0, and midpoint current i_{n0} after injecting u_0 can be expressed as follows:

$$i_{n0} = \sum_{x=A,B,C} d_{x0} i_x, d_{x0} = \begin{cases} \frac{1-(u_x+u_0)}{1-\lambda}, u_x + u_0 \geq \lambda \\ \frac{1+(u_x+u_0)}{1+\lambda}, u_x + u_0 < \lambda \end{cases}. \tag{10}$$

Obviously, as illustrated in Fig. 6, the sinusoidal modulated signals after injecting ZSC must not exceed the modulation index limit, and can be described as

$$1 \geq u_x + u_0 \geq -1 \Rightarrow \begin{cases} u_0 \geq -1 - u_x \\ u_0 \leq 1 - u_x \end{cases}. \tag{11}$$

The aforementioned equation can be simplified to determine the range of ZSC as follows:

$$\begin{cases} u_0 \geq -1 - u_{\min}, u_{\min} = \min(u_A, u_B, u_C) \\ u_0 \leq 1 - u_{\max}, u_{\max} = \max(u_A, u_B, u_C) \end{cases}. \tag{12}$$

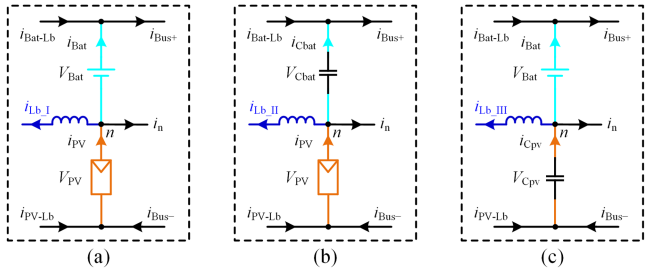

Fig. 10. Equivalent circuits of midpoint *n* during various modes. (a) PV, battery and grid are available. (b) Battery is unavailable. (c) PV is unavailable.

B. Inductor Current Ripple Analysis

The inductor current of improved TPTL-MPC mainly has two parts, which include high-frequency (switch frequency) ripple and low-frequency (grid frequency) ripple. According to Fig. 5, the equivalent circuits of midpoint *n* are shown in Fig. 10 when the grid is available. The high-frequency inductor current ripple $\Delta I_{\rm Lb\_HF}$ is fixed during various modes, and can be calculated by

$$V_{\rm PV} = L_b \frac{\Delta I_{\rm Lb\_HF}}{\Delta t} \Rightarrow \Delta I_{\rm Lb\_HF} = \frac{V_{\rm Bat} V_{\rm PV}}{L_b f_b (V_{\rm Bat} + V_{\rm PV})} \tag{13}$$

where L_b is the inductor, and f_b is the frequency of switches Q_1 and Q_2. Moreover, the low-frequency inductor current ripple during various modes is analyzed as follows.

1) PV, Battery, and Grid are Available: The power relationship of PV, battery, and grid can be described as

$$\begin{aligned} P_G &= P_{\rm ES} + P_{\rm PV} \Rightarrow V_{\rm Bat} I_{\rm Bat} + V_{\rm PV} I_{\rm PV} \\ &= v_A i_A + v_B i_B + v_C i_C \end{aligned} \tag{14}$$

where $I_{\rm Bat}$ and $I_{\rm PV}$ are current of the battery and PV, respectively. According to Kirchhoff's current law (KCL) for node *n*, the inductor low-frequency current $i_{\rm Lb\_I}$ in this mode can be obtained as

$$i_{\rm Lb\_I} = I_{\rm PV} - \frac{v_A i_A + v_B i_B + v_C i_C - V_{\rm PV} I_{\rm PV}}{V_{\rm Bat}} - i_n. \tag{15}$$

2) PV and Grid are Available: Similarly, through the principle of power balance and KCL, the inductor low-frequency current $i_{\rm Lb\_II}$ in this mode can be obtained as

$$P_G = P_{\rm PV} \Rightarrow V_{\rm PV} I_{\rm PV} = v_A i_A + v_B i_B + v_C i_C \tag{16}$$

$$i_{\rm Lb\_II} = I_{\rm PV} - i_n. \tag{17}$$

3) Battery and Grid are Available: Similarly, through the principle of power balance and KCL, the inductor low-frequency current $i_{\rm Lb\_III}$ in this mode can be obtained as

$$P_G = P_{\rm ES} \Rightarrow V_{\rm Bat} I_{\rm Bat} = v_A i_A + v_B i_B + v_C i_C \tag{18}$$

$$i_{\rm Lb\_III} = -\frac{v_A i_A + v_B i_B + v_C i_C}{V_{\rm Bat}} - i_n. \tag{19}$$

Obviously, based on the above-mentioned analysis, it should be noted that the low-frequency ripples of the inductor, PV and battery for improved TPTL-MPC originates from midpoint current i_n.

TABLE I
PROPOSED OPTIMAL ZSCS IN DIFFERENT AREA

Area	ZSCs	Relationship with λ
I	$(\frac{1-u_A}{1-\lambda}i_A+\frac{1+u_B}{1+\lambda}i_B+\frac{1-u_C}{1-\lambda}i_C)/(\frac{i_A}{1-\lambda}+\frac{-i_B}{1+\lambda}+\frac{i_C}{1-\lambda})$	$u_A\geq\lambda$, $u_B<\lambda$, $u_C\geq\lambda$
II	$(\frac{1-u_A}{1-\lambda}i_A+\frac{1+u_B}{1+\lambda}i_B+\frac{1+u_C}{1+\lambda}i_C)/(\frac{i_A}{1-\lambda}+\frac{-i_B}{1+\lambda}+\frac{-i_C}{1+\lambda})$	$u_A\geq\lambda$, $u_B<\lambda$, $u_C<\lambda$
III	$(\frac{1-u_A}{1-\lambda}i_A+\frac{1-u_B}{1-\lambda}i_B+\frac{1+u_C}{1+\lambda}i_C)/(\frac{i_A}{1-\lambda}+\frac{i_B}{1-\lambda}+\frac{-i_C}{1+\lambda})$	$u_A\geq\lambda$, $u_B\geq\lambda$, $u_C<\lambda$
IV	$(\frac{1+u_A}{1+\lambda}i_A+\frac{1-u_B}{1-\lambda}i_B+\frac{1+u_C}{1+\lambda}i_C)/(\frac{-i_A}{1+\lambda}+\frac{i_B}{1-\lambda}+\frac{-i_C}{1+\lambda})$	$u_A<\lambda$, $u_B\geq\lambda$, $u_C<\lambda$
V	$(\frac{1+u_A}{1+\lambda}i_A+\frac{1-u_B}{1-\lambda}i_B+\frac{1-u_C}{1-\lambda}i_C)/(\frac{-i_A}{1+\lambda}+\frac{i_B}{1-\lambda}+\frac{i_C}{1-\lambda})$	$u_A<\lambda$, $u_B\geq\lambda$, $u_C\geq\lambda$
VI	$(\frac{1+u_A}{1+\lambda}i_A+\frac{1+u_B}{1+\lambda}i_B+\frac{1-u_C}{1-\lambda}i_C)/(\frac{-i_A}{1+\lambda}+\frac{-i_B}{1+\lambda}+\frac{i_C}{1-\lambda})$	$u_A<\lambda$, $u_B<\lambda$, $u_C\geq\lambda$

C. Proposed Optimal ZSC Injection Method

It can be seen from (15), (17), and (19) that the inductor current ripple i_{Lb} comes entirely from midpoint current i_n, regardless of operational modes for the improved TPTL-MPC. Therefore, in order to suppress and reduce the low-frequency voltage and current ripples, it is equivalent to eliminating ripple of i_n. According to (10), the i_n can be changed by injecting ZSC u_0. In order to reduce voltage and current ripples, the u_0 can be injected into u_x to make $i_n=0$. As illustrated in Fig. 6, the u_x can be divided into six areas (Area-I to Area-VI) based on relationship between u_x and λ. Combining Fig. 6 and (10), assuming that there is no change in area division before and after injecting u_0, the u_0 can be calculated for Area-I

$$i_{n0}=\sum_{x=A,B,C}d_{x0}i_x=\frac{1-(u_A+u_0)}{1-\lambda}i_A+\frac{1+(u_B+u_0)}{1+\lambda}i_B+\frac{1-(u_C+u_0)}{1-\lambda}i_C. \tag{20}$$

The u_0 in Area-I can be simplified and obtained as

$$\mathrm{Area-I}: u_0=\frac{\frac{1-u_A}{1-\lambda}i_A+\frac{1+u_B}{1+\lambda}i_B+\frac{1-u_C}{1-\lambda}i_C}{\frac{i_A}{1-\lambda}+\frac{-i_B}{1+\lambda}+\frac{i_C}{1-\lambda}},\ u_A\geq\lambda,u_B<\lambda,u_C\geq\lambda. \tag{21}$$

Similarly, the proposed optimal ZSC u_0 of other areas can be obtained with same way, as shown in Table I. In addition, the i_n is equal to zero if $u_A>\lambda$, $u_B>\lambda$, $u_C>\lambda$, or $u_A<\lambda$, $u_B<\lambda$, $u_C<\lambda$. And the u_0 is also equal to zero in above-mentioned two cases.

It is very important to note that the area division in Table I is determined based on the intersection points of the modulated wave $u_x(x=A,B,C)$ and λ. However, there is a problem that near the intersection of u_x and λ, the area division is inconsistent before and after preliminary injection of u_0, as shown in Fig. 12. Using the proposed ZSC (calculated by Table I), after the preliminary calculation and injection into the original sinusoidal modulated signals, $u_{x1}(x=A,B,C)$ is obtained. According to the division in Table I, in the green area of Fig. 12, the division is inconsistent before and after the injection of the first ZSC. Therefore, after one ZSC calculation, the low-frequency ripple in the green area of $u_{x1}(x=A,B,C)$ cannot be effectively reduced.

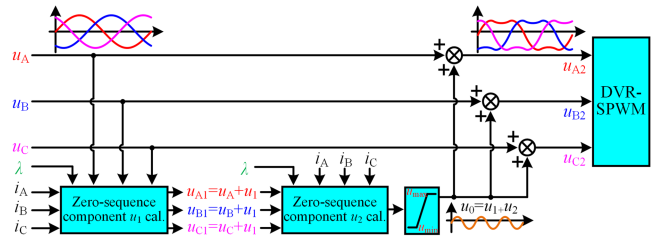

Fig. 11. Scheme of the proposed optimal ZSC injection method.

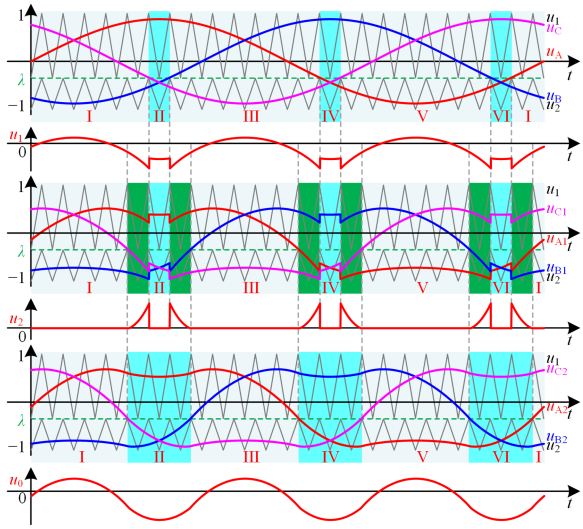

Fig. 12. Key waveforms of proposed optimal ZSC injection method.

In order to solve above-mentioned problem, the u_0 consists of two parts with using the proposed optimal ZSC in Table I. The scheme of the proposed optimal ZSC injection method is shown in Fig. 11, and its key waveforms are illustrated in Fig. 12. First of all, the preliminary ZSC u_1 is calculated through Table I, which can make the midpoint current i_n to zero in the part of the same area before and after injection of u_1. And the preliminary modulated signals u_{x1} are equivalent to u_x+u_1. Obviously, the area division in the green area of u_{A1}, u_{B1}, u_{C1} (as shown in Fig. 12) is inconsistent before and after injection of u_1. Second, the secondary ZSC u_2 is calculated through Table I, which can make the midpoint current i_n of the green area of u_{A1}, u_{B1}, u_{C1} to zero. Finally, the proposed optimal ZSC u_0 is equivalent to u_1+u_2, which needs to be limited within the range of (12). And the three-phase sinusoidal modulated signals u_{A2}, u_{B2}, u_{C2} after injection of the proposed optimal u_0 is shown in Fig. 12.

In addition, according to Table I, it can also be seen that the proposed optimal ZSC is not related to the peak current of the grid, but is related to the displacement angle between grid voltage and current. Since the proposed optimal ZSC injection method includes the phase information of the grid current, it can reduce the low-frequency voltage and current ripples of improved TPTL-MPC at different power factors (PF) within the

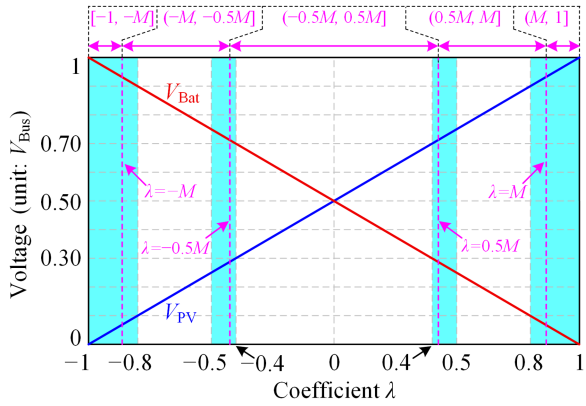

Fig. 13. Relationship between the battery voltage, the PV voltage and coefficient λ.

range [as shown in (12)] of the proposed optimal ZSC. Meanwhile, the proposed optimal ZSC injection method also contains voltage information [as shown in (5)] of the PV and battery. As illustrated in Figs. 5 and 10 along with the corresponding analysis, the low-frequency ripple originates entirely from the midpoint current in all operation modes of improved TPTL-MPC. By applying the proposed optimal ZSC injection method, the midpoint current ripple in all operation modes depicted in Fig. 5 can theoretically be eliminated. Therefore, the inductor current ripples can be effectively reduced, and the current ripples of PV and battery for the improved TPTL-MPC can also be suppressed in various operational modes. In addition, the actual effectiveness of low-frequency ripple suppression based on the proposed optimal ZSC method will be demonstrated in the experimental validation of Section V.

D. Limitation Analysis of Coefficient λ for the Proposed Optimal ZSC Injection Method

Based on the principle that the bus voltage V_{Bus} is equal to the sum of the battery voltage V_{Bat} and the PV voltage V_{PV} for the proposed TPTL-MPC, the coefficient λ in (5) can be calculated as follows:

$$\lambda = \frac{2V_{\mathrm{PV}}}{V_{\mathrm{Bus}}} - 1 = 1 - \frac{2V_{\mathrm{Bat}}}{V_{\mathrm{Bus}}}, (V_{\mathrm{PV}} \le V_{\mathrm{Bus}}, V_{\mathrm{Bat}} \le V_{\mathrm{Bus}}). \quad (22)$$

Theoretically, the range of the coefficient λ is [−1, 1]. Moreover, when any two sinusoidal modulated signals (u_A, u_B, u_C) are equal, the values of corresponding sinusoidal modulated signals are 0.5 M or −0.5 M. And the maximum and minimum values of sinusoidal modulated signals are M and $-M$. Therefore, based on the relationship of modulation index M and coefficient λ, the range of the coefficient λ can be divided into six segments, which includes [1, $-M$], ($-M$, $-M$/2], ($-M$/2, 0], (0, M/2], (M/2, M], (M, 1].

According to (22), the battery voltage and PV voltage can be expressed

$$V_{\mathrm{PV}} = \frac{1+\lambda}{2} V_{\mathrm{Bus}}, V_{\mathrm{Bat}} = \frac{1-\lambda}{2} V_{\mathrm{Bus}}. \quad (23)$$

Based on (23), Fig. 13 shows the relationship between the battery voltage, the PV voltage and coefficient λ. It should be noted that the too small M will result in low utilization rate of dc bus voltage. Generally, the selection of M needs to take into account both the voltage regulation margin and the utilization rate of dc bus voltage. The M ranging from 0.8 to 1 is selected as the representative value for analysis (i.e., the light blue area in Fig. 13). The theoretical analysis regarding the validity of proposed optimal ZSC injection method in each coefficient λ range is presented as follows.

1) *λ∈(−0.5 M, 0.5 M]:* The sinusoidal modulated signals can be divided into six areas (Area-I to Area-VI in Table I) based on relationship between sinusoidal modulated signals and λ. In this range of coefficient λ, the proposed optimal ZSC injection method can effectively reduce the low-frequency voltage and current ripples of improved TPTL-MPC.
2) *λ∈(−M, −0.5 M], or λ∈(0.5 M, M]:* For λ∈(−M, −0.5 M], the sinusoidal modulated signals can be divided into four areas (Area-I, Area-III, Area-V, and the special area that sinusoidal modulated signals are all greater than λ) based on relationship between sinusoidal modulated signals and λ. Similarly, for λ∈(0.5 M, M], the sinusoidal modulated signals can be divided into four areas (Area-II, Area-IV, Area-VI, and the special area that sinusoidal modulated signals are all less than λ).
3) *λ∈[−1, −M], or λ∈(M, 1]:* For λ∈[−1, −M], the sinusoidal modulated signals are all greater than λ, only the battery directly supplies power to the ac side. Similarly, for λ∈(M, 1], the sinusoidal modulated signals are all less than λ, only the PV directly supplies power to the ac side. Therefore, the inverter unit is equivalent to the traditional three-phase full-bridge structure, and the midpoint current is the current of the dc bus, whose ripple is relatively small in this case. And the proposed optimal ZSC injection method cannot affect the midpoint current.

It should be noted that the above-mentioned detailed analysis covered all possible the range of the coefficient λ. However, in order to utilize the advantages of the T-type three-level NPC unit in practical applications, the reasonableness between PV voltage and battery voltage needs to be carefully considered to ensure that the dc port voltage ratio λ remains within an appropriate range. When the bus voltage remains constant, a larger voltage difference between the PV and battery causes the T-type NPC unit to operate more similarly to a conventional two-level inverter, resulting in higher THD of grid current. Meanwhile, the greater gain in the bidirectional buck-boost unit leads to lower efficiency. The following is the critical threshold points (λ = 0.5 M and λ = M) for the range of the coefficient λ. The conditions for λ = 0.5 M and λ = M are expressed as follows:

$$\begin{cases} V_{\mathrm{PV}} = \frac{2+M}{4} V_{\mathrm{Bus}}, V_{\mathrm{Bat}} = \frac{2-M}{4} V_{\mathrm{Bus}}, \text{when } \lambda{=}0.5M \\ V_{\mathrm{PV}} = \frac{1+M}{2} V_{\mathrm{Bus}}, V_{\mathrm{Bat}} = \frac{1-M}{2} V_{\mathrm{Bus}}, \text{when } \lambda{=}M \end{cases}. \quad (24)$$

Therefore, when λ is in the range of (−M, −0.5 M] or (0.5 M, M], the voltage difference between the PV and battery is significant [i.e., $V_{\mathrm{PV}} \ge 2.33\ V_{\mathrm{Bat}} \sim 3\ V_{\mathrm{Bat}}$, according to (24)]. The power loss of bidirectional buck-boost unit is relatively

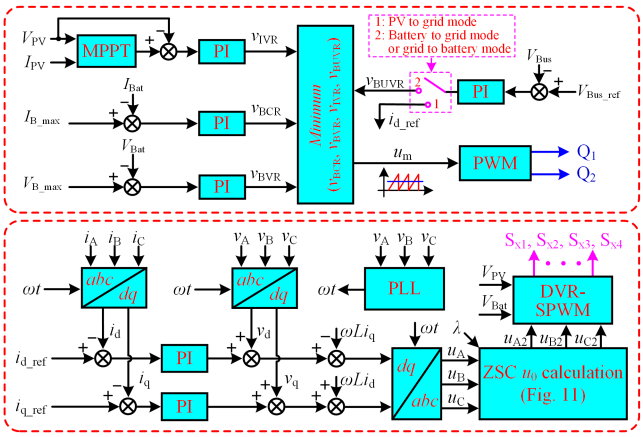

Fig. 14. Control strategy of the improved TPTL-MPC.

large, which leads to lower overall efficiency of the improved TPTL-MPC and higher THD of grid current. In the parameter designs, the coefficient λ should be avoided to be greater than 0.5 M. In addition, when λ is in the range of $[-1, -M]$ or $(M, 1]$, the improved TPTL-MPC is only supplied by the PV or battery to grid, and the voltage difference between the PV and battery is very large [i.e., $V_{\rm PV} \geq 9\, V_{\rm Bat}$, according to (24)]. This situation is unacceptable and should be avoided in the parameter design.

E. Control Strategy of Improved TPTL-MPC

To achieve power control among the PV, battery, and grid, the control strategy of improved TPTL-MPC is investigated, as shown in Fig. 14. There are four control objectives, including the MPPT control for PV, constant dc bus voltage control, control of battery charging and discharging, and grid-connected control. Specifically, the input voltage regulator (IVR) is used for MPPT control. The battery current regulator (BCR) and battery voltage regulator (BVR) are used for the battery management. The bus voltage regulator (BUVR) is used for constant dc bus voltage control in case of nonoperation of PV or battery. $V_{B\_\max}$ and $I_{B\_\max}$ are maximum voltage and current references of battery, and $V_{\rm Bus\_ref}$ is reference of dc bus voltage. The minimum value of $v_{\rm IVR}$, $v_{\rm BVR}$, $v_{\rm BCR}$ and $v_{\rm BUVR}$ is selected to control buck-boost unit for different operational scenarios. In addition, dq-decoupled grid-connected control strategy is adopted in this article. The phase-locked loop is realized by the grid voltage, which provides phase information for Park transformation. The reference values of d-axis and q-axis grid current ($i_{d\_\rm ref}$, $i_{q\_\rm ref}$) are realized through proportional-integral (PI) closed-loop control and decoupled component, which can ensure the desired power injection into the grid. As illustrated in Fig. 5, the circuit states of the improved TPTL-MPC during various modes are divided into four types, and their control strategy can be analyzed as follows, respectively.

1) *PV to battery:* the minimum value of $v_{\rm IVR}$, $v_{\rm BVR}$, and $v_{\rm BCR}$ is selected to generate duty cycle to control Q_2 of the bidirectional buck-boost unit, which can match the PV and battery voltage variations, and realize MPPT of the PV or power control of the battery.
2) *PV to grid:* the IVR is used for the MPPT control of PV, and the output of BUVR is also selected to reference value of grid-connected current to maintain the dc bus voltage constant. The dq-decoupled grid-connected control strategy is adopted to realize separately control of the active power and reactive power of the grid.
3) *Battery to grid, or grid to battery:* the minimum value of $v_{\rm BUVR}$, $v_{\rm BVR}$, and $v_{\rm BCR}$ is selected to generate the duty cycle to control bidirectional buck-boost unit, and constant the dc bus voltage. It is worth noting that the primary objective for the bidirectional buck-boost unit is to achieve the bus voltage control. The inverter state and rectifier state can be realized by d-axis reference value of grid-connected control strategy.
4) *PV to battery and grid, or PV and battery to grid, or PV and grid to battery:* the minimum value of $v_{\rm IVR}$, $v_{\rm BVR}$, and $v_{\rm BCR}$ is selected to generate the duty cycle to control bidirectional buck-boost unit in multiport mode. It is worth noting that the primary objective for the bidirectional buck-boost unit is to achieve the bus voltage control or the MPPT of PV.

When the improved TPTL-MPC operates in battery to grid, or grid to battery, the minimum value of $v_{\rm BUVR}$, $v_{\rm BVR}$, and $v_{\rm BCR}$ is selected to generate the duty cycle to control bidirectional buck-boost unit, and constant the dc bus voltage. When the battery current $I_{\rm Bat}$ is less than the set maximum current $I_{B\_\max}$, the difference between $I_{\rm Bat}$ and $I_{B\_\max}$ is greater than zero. After PI control, the generated $v_{\rm BCR}$ gradually reaches its maximum value. However, when the battery current $I_{\rm Bat}$ exceeds the set maximum current $I_{B\_\max}$, the difference between $I_{\rm Bat}$ and $I_{B\_\max}$ is less than zero. After PI control, the generated $v_{\rm BCR}$ rapidly decreases, thereby reducing the duty cycle of the switches for the bidirectional buck-boost unit, which protects battery from overcharging or overdischarging. The analysis of $v_{\rm BVR}$ is similar to that of the above $v_{\rm BCR}$.

In summary, among the above four types, when the PV is available, the $V_{\rm IVR}$ controls the bidirectional buck-boost unit to achieve MPPT of PV, while when the PV is unavailable, the $V_{\rm BUVR}$ controls the bidirectional buck-boost unit to achieve the bus voltage control. The relinquishment of bus voltage control signal $v_{\rm BUVR}$ or MPPT control signal $v_{\rm IVR}$ occurs only when the battery reaches its safe charging and discharging threshold ($I_{B\_\max}$ or $V_{B\_\max}$), prioritizing the secure management of charging and discharging operations for the battery [31].

F. Hardware Design of Improved TPTL-MPC

The hardware design of the improved TPTL-MPC includes inductor (L_b), switches (S_{A1}–S_{A4}, S_{B1}-S_{B4}, S_{C1}–S_{C4}, Q_1–Q_2), and input capacitors ($C_{\rm Bat}$, $C_{\rm PV}$). And the detailed hardware design is illustrated as follows.

According to (13), the coefficient of inductor L_b current ripple is defined as δ. And the inductor can be expressed

$$L_b \geq \frac{V_{\rm Bat}V_{\rm PV}}{\Delta I_{\rm Lb\_HF} f_b V_{\rm Bus}} = \frac{V_{\rm Bat}V_{\rm PV}}{\delta I_{\rm Lb\_HF} f_b V_{\rm Bus}}. \tag{25}$$

TABLE II
MAXIMUM VOLTAGE AND CURRENT STRESSES OF THE SWITCHES

Switches	Maximum drain-source voltage	Maximum drain-source current
Q_1–Q_2	$V_{\text{Bat}}+V_{\text{PV}}$	$I_{\text{PV}}+\dfrac{P_{\text{G\_max}}+P_{\text{PV}}}{V_{\text{Bat}}}-i_{\text{n}}$
S_{A1}, S_{A4}, S_{B1}, S_{B4}, S_{C1}, S_{C4}	$V_{\text{Bat}}+V_{\text{PV}}$	I_{Gpk}
S_{A2}, S_{A3}, S_{B2}, S_{B3}, S_{C2}, S_{C3}	$S_{A2}, S_{B2}, S_{C2}: V_{\text{Bat}}$ $S_{A3}, S_{B3}, S_{C3}: V_{\text{PV}}$	I_{Gpk}

For the PV and grid to battery mode, the maximum inductor current can be calculated by

$$i_{\text{Lb\_max}} = I_{\text{PV}} + \frac{P_{G\_\text{max}} + P_{\text{PV}}}{V_{\text{Bat}}} - i_n \tag{26}$$

where P_{G_max} is the maximum grid power for rectifier state.

Therefore, the minimum inductor and maximum inductor current [as shown in (25) and (26)] can serve as reference for hardware design of inductor L_b.

For improved TPTL-MPC, the maximum voltage and current stresses of the switches (S_{A1}–S_{A4}, S_{B1}–S_{B4}, S_{C1}–S_{C4}, Q_1–Q_2) can be summarized in Table II, which can serve as a reference for hardware design of switch selections. The maximum current of T-type NPC unit is the peak grid current. Moreover, the maximum currents I_{Q1_max}, I_{Q2_max} of switches Q_1, Q_2 can be calculated as follows:

$$I_{Q1\_\text{max}} = I_{Q2\_\text{max}} = i_{\text{Lb\_max}} = I_{\text{PV}} + \frac{P_{G\_\text{max}} + P_{\text{PV}}}{V_{\text{Bat}}} - i_n. \tag{27}$$

For the improved TPTL-MPC, the voltage ripple of input capacitor originates from the midpoint current ripple. In the case of single input and single output (the PV or battery is unavailable), the most extreme situation is that all the midpoint current ripple flows to the input capacitor. The midpoint current $i_n(t)$ is expressed in (9). Moreover, the frequency of the midpoint current ripple is three times that of the grid frequency, without ZSC injection. Assuming the ripple coefficient of the capacitor voltage is β and the peak value of the midpoint current ripple is I_{npk}. According to (9) and the relationship between the capacitor voltage and current, the capacitor of the battery port can be calculated as follows:

$$\Delta V_{\text{Bat}} = \frac{1}{C_{\text{Bat}}}\int i_n(t)dt = \beta V_{\text{Bat}} \Rightarrow C_{\text{Bat}} \geq \frac{\int i_n(t)dt}{\beta V_{\text{Bat}}} = \frac{I_{\text{npk}}}{6\beta\pi f_{\text{o}} V_{\text{Bat}}}. \tag{28}$$

Similarly, the capacitor of PV port can be calculated by the above-mentioned equation.

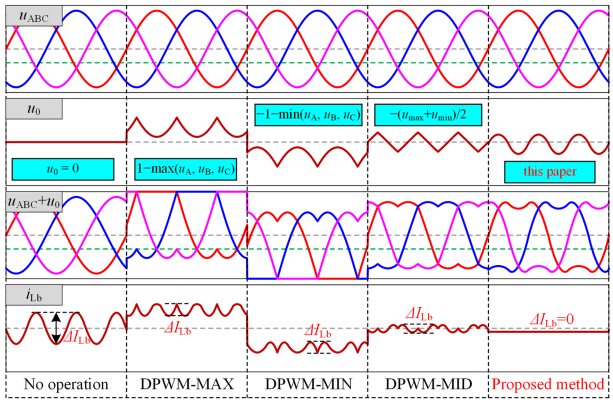

Fig. 15. Key waveforms of inductor low-frequency current ripples ΔI_{Lb} and i_n in different ZSC u_0.

IV. PERFORMANCE COMPARISON AND ANALYSIS

A. Comparison With Other ZSC Injection Methods

In order to compare with the other typical ZSC injection methods, the DPWM-MAX, DPWM-MIN, and DPWM-MID are selected for the improved TPTL-MPC, as shown in Fig. 15. In the exiting literatures [28], [29], [30], they are defined as follows, respectively

$$\begin{cases} \text{DPWM}-\text{MAX}: u_0 = 1 - u_{\text{max}} \\ \text{DPWM}-\text{MIN}: u_0 = -1 - u_{\text{min}} \\ \text{DPWM}-\text{MID}: u_0 = -(u_{\text{max}} + u_{\text{min}})/2 \end{cases}. \tag{29}$$

Combined with (11) and (12), it is obvious that the DPWM-MAX and DPWM-MIN are maximum and minimum values of ZSCs, respectively. On the other hand, for the traditional three-phase two-level or three- level inverters, the space-vector PWM (SVPWM) can be equivalent to inject ZSC u_0 (DPWM-MID) into the sinusoidal modulated signal. It can be seen from Fig. 15 that the proposed optimal ZSC injection method can reduce the low-frequency voltage and current ripples of the inductor, PV, and battery for improved TPTL-MPC, comparing with other typical ZSC injection methods. Consequently, by injecting proposed optimal ZSC, the low-frequency ripple of midpoint current i_n is eliminated, thereby reducing the voltage and current ripples on the dc side of improved TPTL-MPC. If SVPWM or space-vector-based zero-sequence injection is used, by applying the proposed optimal ZSC injection method, the optimal ZSC u_0 will also be generated, thereby modifying the original modulation wave.

According to (10) and (15), in multiport mode, the relationship between the inductor low-frequency current ripples and the grid power, as well as the displacement angle φ is illustrated in Fig. 16 for different u_0. And the circuit parameters are given in Table IV. Fig. 16(a) illustrates the relationship between average inductor current and grid power in different u_0, which indicates that the energy transmitted by the inductor at different u_0 and grid power. It can be seen that the average inductor current of the proposed optimal ZSC injection method is slightly less than noninjected ZSC. The relationship between the inductor

TABLE III
COMPARISON AMONG OTHER DC—DC–AC MPCS

Structures of MPC ased on three-phase 3L-NPC	Port voltage constraints	References & Topology of 3L-NPC	Rated voltage: V_{PV}, V_{Bat} $V_{G\text{-}RMS}/f_o$	Switching frequency	Modulation & Control complexity	Degree of coupling	V/I ripples of dc ports	Cost & power limitation	Peak efficiency (multiport mode) @Rated power
Structure I 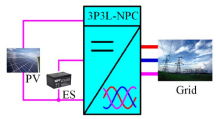	$V_{PV} > V_{Bat}$ $V_{PV} > 2V_{Gpk}$	[19] & Diode-NPC	180–210 V 90–160 V 55V/60 Hz	10 kHz	Virtual SVPWM & Complex	High	Large	Low & Large	N/A @P_{PV} = 780 W, P_G = 1000 W
Structure II 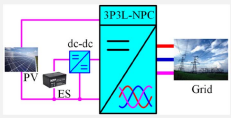	$V_{PV} > V_{Bat}$ $V_{PV} > 2V_{Gpk}$	[22] & T-type NPC	600 V N/A N/A, 50 Hz	3L-NPC: 20 kHz dc–dc: 20 kHz	RCMV-DSVPWM & Complex	Medium	Medium	Medium & Medium	N/A @P_{PV} = N/A, P_G = 6000 W
Structure III 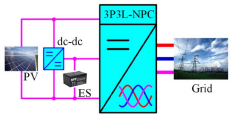	$V_{PV} > V_{Bat}$ $V_{PV} > 2V_{Gpk}$	[23] & Diode-NPC	180V–210 V 100V–150 V 55V/60 Hz	3L-NPC: 20 kHz dc–dc: 50 kHz	Modified SVPWM & Complex	Medium	Medium	Medium & Medium	95.3% @P_{PV} = 1000 W, P_G = 500 W
Improved structure 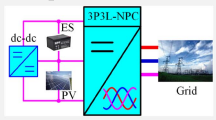	**$V_{PV} + V_{Bat}$ $> 2V_{Gpk}$**	**This article & T-type NPC**	**72 V–96 V 96 V–120 V 55 V/50 Hz**	**3L–NPC: 20 kHz dc–dc: 50 kHz**	**DVR-SPWM (using proposed optimal ZSC) & Simple**	**Low**	**Lower**	**Medium & Small**	**96.5% @P_{PV} = 600 W, P_G = 1000 W**

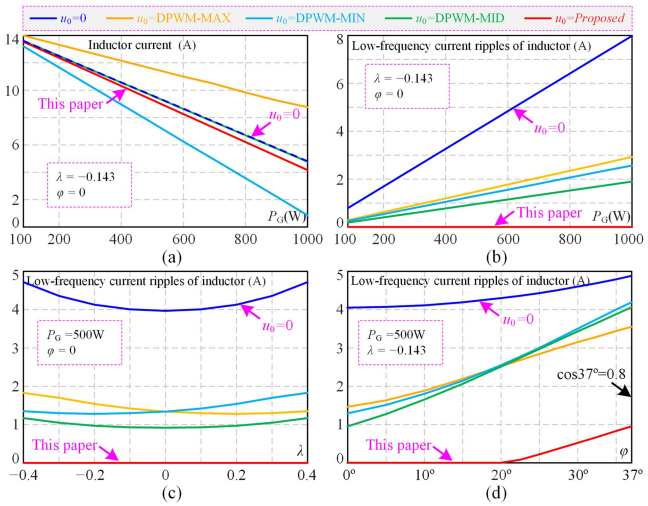

Fig. 16. (a) Relationship between the inductor current and grid power. Relationship between the inductor low-frequency current ripple and (b) grid power, and (c) coefficient λ, and (d) displacement angle (PF = 0.8–1).

TABLE IV
CIRCUIT PARAMETERS OF THE EXPERIMENTAL PROTOTYPE

Parameters	Value
Rated grid power P_G	1000 W
Rated PV power P_{PV}	600 W
Voltage of PV, battery, and grid	V_{PV} = 72–96 V, V_{Bat} = 96–120 V $V_{G\text{-}RMS}$ = 55 V
Frequency of f_o, f_s, f_b	50 Hz, 20 kHz, 50 kHz
Input capacitors	C_{Bat} = 2 mF, C_{PV} = 2 mF
Inductor L_b	500 μH
Switches Q_1-Q_2, S_{x1}-S_{x4}	IRFP4137PBF
Filters L_{fA}, L_{fB}, L_{fC}	L_{fA} = L_{fB} = L_{fC} = 3 mH
Control period	50 μs
Controller	TMS320F280049C

low-frequency current and grid power are shown in Fig. 16(b) with unity PF. The proposed optimal ZSC injection method can minimize the inductor current ripple in the full load range. It can also be observed from Table I that the proposed optimal ZSC is independent of the I_{Gpeak}. In addition, the relationship between the inductor low-frequency current ripples and port voltage coefficient λ are shown in Fig. 16(c) with unity PF, where P_G = 500 W. Moreover, it can be seen form Fig. 16(d) that the proposed optimal ZSC injection method can completely eliminate inductor low-frequency current ripple within certain PF range (such as 0.8–1), where P_G = 500 W. Compared with other traditional ZSC injection methods, the inductor current ripple is greatly reduced in the different P_G, PF, and λ.

On the other hand, it is important to highlight that the current ripple source of both the inductor and dc ports for the improved TPTL-MPC originates from the ripple of midpoint current i_n. The amplitude and phase of midpoint current can be adjusted by injecting ZSC. According to the above analysis and Fig. 16(d), when the calculated ZSC exceeds the limit in (12), the proposed optimal ZSC injection method cannot completely eliminate the inductor current ripple. However, it can still maintain a minimum inductor current ripple comparing with other ZSC injection methods. The actual effectiveness of low-frequency ripple suppression based on the proposed optimal ZSC injection method will be demonstrated for different PF in the experimental validation of Section V. In addition, the range of PF and λ, and other parameters of the improved TPTL-MPC can be designed in

advance, and the required modulation range can be reserved. The low-frequency current ripple of inductor, and voltage and current ripples of dc input port can be reduced through reasonable parameter design process.

B. Comparison With Other DC–DC–AC MPCs

In order to compare the characteristics of several structures, the comparison results among other dc–dc–ac MPCs are given in Table III, which are provided detailed comparison with respect to similar solutions, in terms of topological architecture, topology of three-phase 3L-NPC, the port voltage constraints, rated parameters, modulation, control complexity, the degree of coupling, voltage and current ripple of dc ports, cost, and the efficiency of MPC. Obviously, the improved structure exhibits relatively relaxed port voltage constraints.

Among the several structures in Table III, structure I has been popularly studied in existing literature due to its simple topology, high integration degree, and low cost. Based on structure I, the structure II and structure III are relatively balanced in the various key comparison parameters. However, there are still problems for above three structures, such as voltage and current (V/I) ripples at dc ports, high coupling degree, and relatively complex modulation and control strategy. The improved structure adopts the proposed optimal ZSC injection method based on the DVR-SPWM, with eliminating inductor current ripple and also reducing V/I ripples of dc ports. And its control strategy is approximately decoupled in control loop of ac-side and dc-side. Moreover, the improved TPTL-MPC has a lower THD of grid current and a higher overall efficiency. Therefore, it can be seen from the comparison results in Table III and the above analysis that the improved structure, combined with the proposed DVR-SPWM, the proposed optimal ZSC injection method, and the control strategy, has excellent performance.

Notably, the comprehensive performance metrics (such as efficiency, voltage and current ripples under dynamic conditions where grid power varies from 0 to 1000 W) are not reported in [19], [22], and [23]. The rigorous and quantitative comparison with existing MPCs remain inherently challenging. And the comparison presented in Table III is restricted to qualitative topological features, with numerical values for switching frequency, efficiency, voltage, and power rating provided solely as indicative characteristics.

V. Experimental Verification

In order to further verify the steady-state and dynamic-state performance, the experimental platform of improved TPTL-MPC is shown in Fig. 17, and its circuit parameters and specifications are given in Table IV. The grid simulator (*ITECH IT7900P*), battery simulator (*Chroma 62180D-1800*), and PV simulator (*Chroma 62150H-600S*) are used for emulating the grid, battery, and PV, respectively. Consequently, the experimental prototype is built to verify the effectiveness and correctness of the improved TPTL-MPC, DVR-SPWM, proposed optimal ZSC injection method and control strategy.

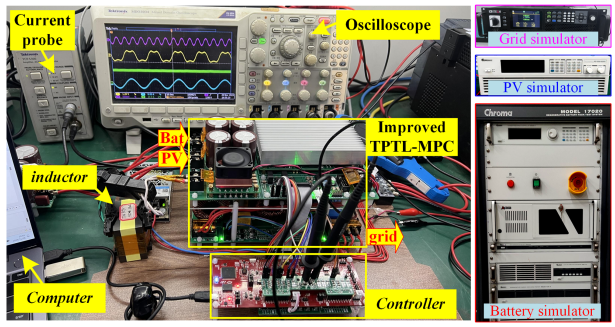

Fig. 17. Experimental platform of improved TPTL-MPC.

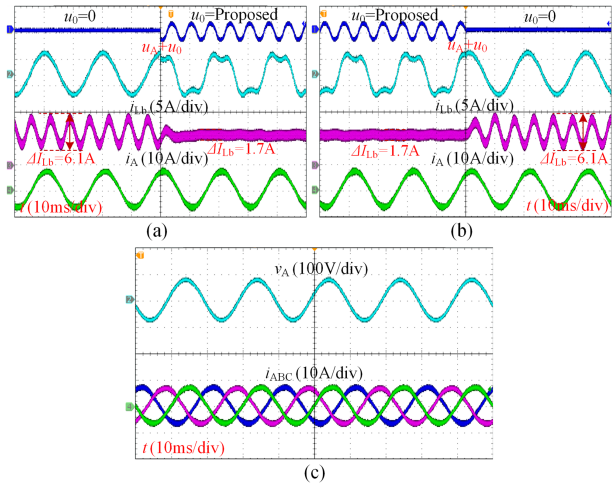

Fig. 18. Steady-state waveforms of u_0, u_A+u_0, i_{Lb}, i_A when (a) u_0 switches from 0 to the proposed optimal ZSC injection method, (b) u_0 switches from the proposed optimal ZSC injection method to 0, and (c) steady-state waveforms of v_A, i_A, i_B, i_C.

A. Steady-State Performance

Fig. 18(a) and (b) present steady-state experimental results when the $u_0 = 0$ and proposed optimal ZSC injection method. It is worth noting that the inductor current ripple primarily consists of low-frequency (grid frequency) ripple and high-frequency (switch frequency) ripple. And the inductor current ripple decreases from 6.1 A to 1.7 A through the proposed optimal ZSC. Obviously, the inductor low-frequency current ripple is basically eliminated by adopting proposed u_0. The steady-state experimental results of grid voltage and current under proposed optimal ZSC injection method are illustrated in Fig. 18(c). The battery voltage and PV voltage (maximum power point) are 96 V and 72 V. Therefore, the bus voltage is 168 V, and the dc port voltage coefficient λ is equal to -0.143 according to (5). The measured experimental THD of i_G is less than 1.5%. The grid current is stable, and grid power is 800 W in multiport mode. The experimental results also demonstrate that, when the voltages of two dc ports are unequal, the proposed DVR-SPWM can still achieve relatively small THD of grid current.

Fig. 19 illustrates the steady-state waveforms of u_0, $u_{\mathrm{A}}+u_0$, i_{Lb}, i_A, and I_{PV}, I_{Bat}, v_A, i_A in different u_0 with PF $= 1$ and PF $= 0.8$, respectively. The grid power set is 800 W, and the

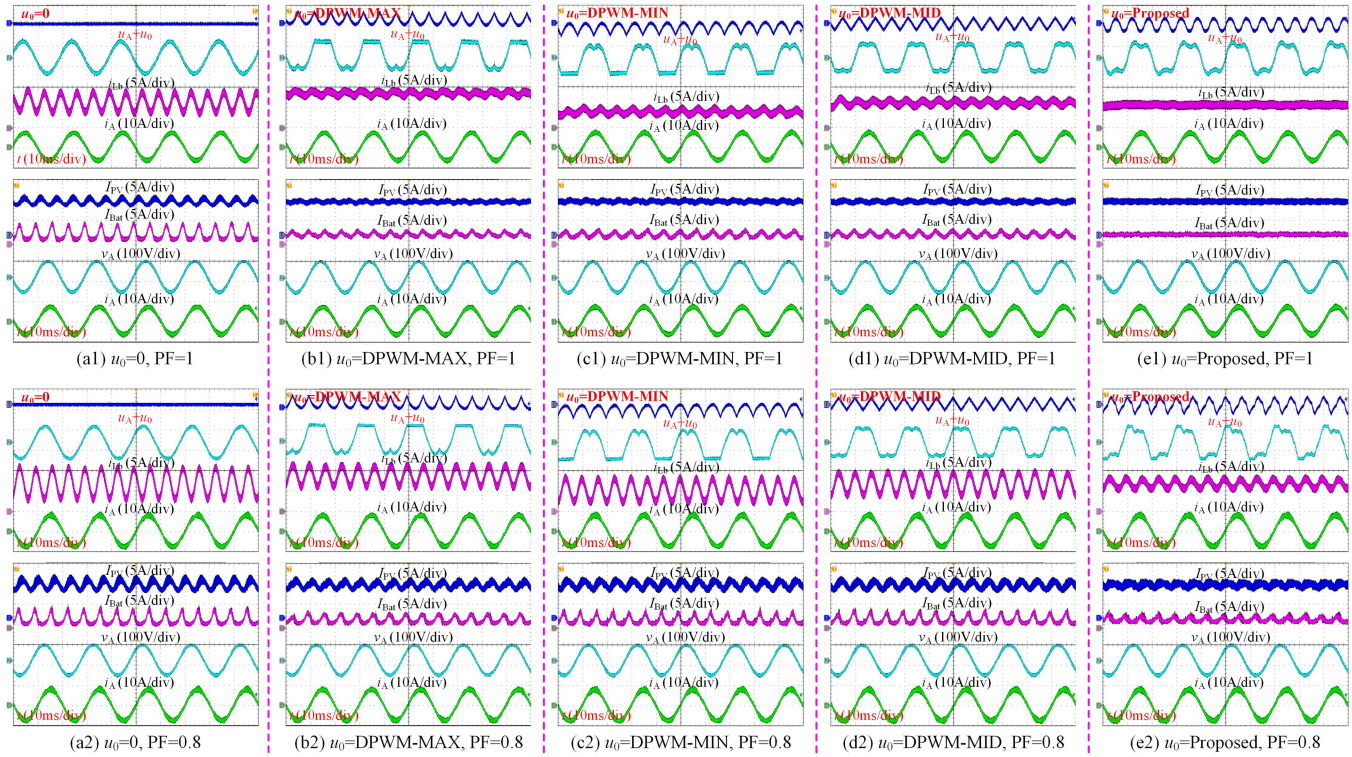

Fig. 19. Steady-state waveforms of u_0, u_A+u_0, i_{Lb}, i_A, and I_{PV}, I_{Bat}, v_A, i_A in different u_0 with PF = 1 and PF = 0.8, respectively. (a1) and (a2) $u_0 = 0$. (b1) and (b2) u_0 = DPWM-MAX. (c1) and (c2) u_0 = DPWM-MIN. (d1) and (d2) u_0 = DPWM-MID. (e1) and (e2) u_0 = proposed optimal ZSC injection method.

PV operates at the maximum power point (600 W). Therefore, the power that the battery needs to replenish exceeds 200 W (considering power loss). When PF = 1 (displacement angle $\varphi = 0°$), obviously, the proposed optimal ZSC injection method can basically eliminate the low-frequency current ripples of the inductor, PV, and battery. When PF = 0.8 (displacement angle $\varphi = 37°$), the proposed optimal zero-sequence injection method cannot eliminate the low-frequency current ripples, and the current ripples of the inductor, the battery, and the PV by adopting the proposed optimal ZSC injection method are significantly reduced, comparing with other ZSC injection methods. According to Fig. 19(a2)–(e2), when PF = 0.8, the magnitudes of inductor current ripple from large to small are respectively: $u_0 = 0 > u_0$ = DPWM-MIN $> u_0$ = DPWM-MID $> u_0$ = DPWM-MAX $> u_0$ = Proposed method. Therefore, it can be seen from Figs. 16 and 19 that the experimental results are consistent with the theoretical analysis.

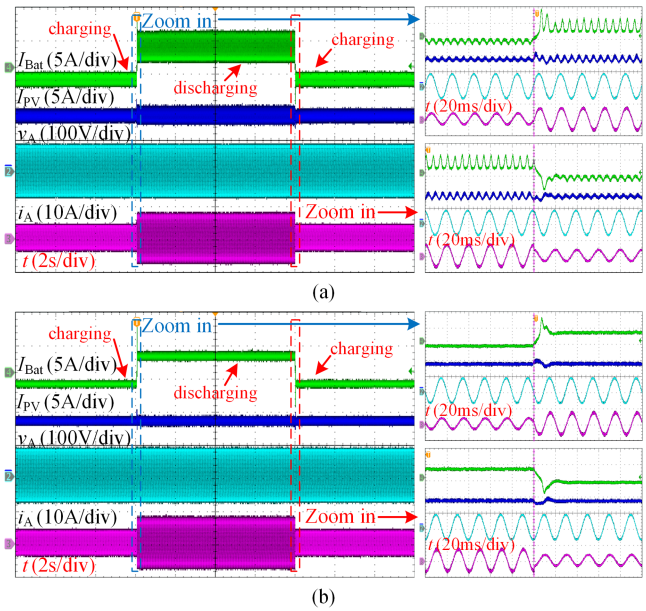

Fig. 20. Dynamic-state waveforms of I_{Bat}, I_{PV}, v_A, i_A when P_G steps between 400 and 800 W. (a) $u_0 = 0$. (b) u_0 = proposed optimal ZSC injection method.

B. Dynamic-State Performance

The dynamic-state experimental waveforms of I_{Bat}, I_{PV}, v_A, and i_A during P_G variation are illustrated in Fig. 20(a) and (b), when $u_0 = 0$ and the proposed optimal ZSC injection method, respectively. The PV remains stable and constant (600 W) as P_G changes among 400 and 800 W. When P_G increases to 800 W, the battery is discharge (about 200 W), whereas the battery gets charged (about −200 W) when the P_G decreases to 400 W. The experimental results demonstrate that P_G variation has not impact on PV, as battery can promptly compensate for power deficiency. By comparing Fig. 20(a) and (b), the current ripples of battery and PV for the proposed optimal ZSC injection method are smaller than without ZSC injection in the steady-state performance. The smaller current ripples have better adaptability and stability for battery and PV. Moreover, the fast

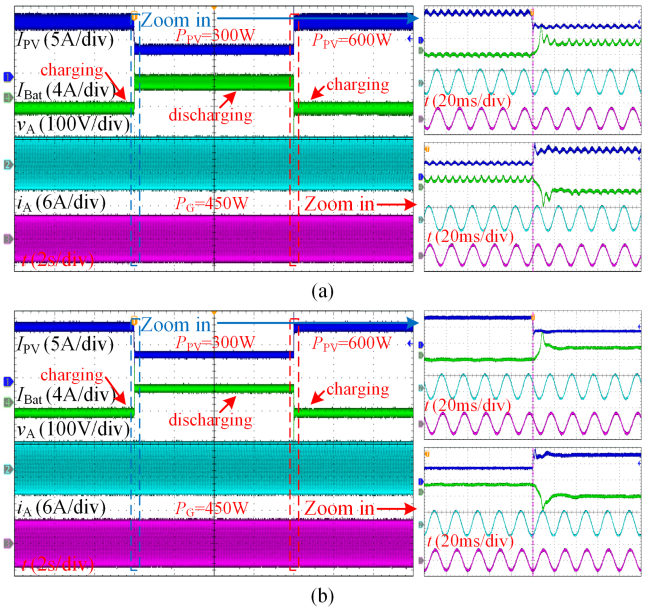

Fig. 21. Dynamic-state waveforms of I_{Bat}, I_{PV}, v_A, i_A when P_{PV} steps between 300 and 600 W. (a) $u_0 = 0$. (b) $u_0 =$ proposed optimal ZSC injection method.

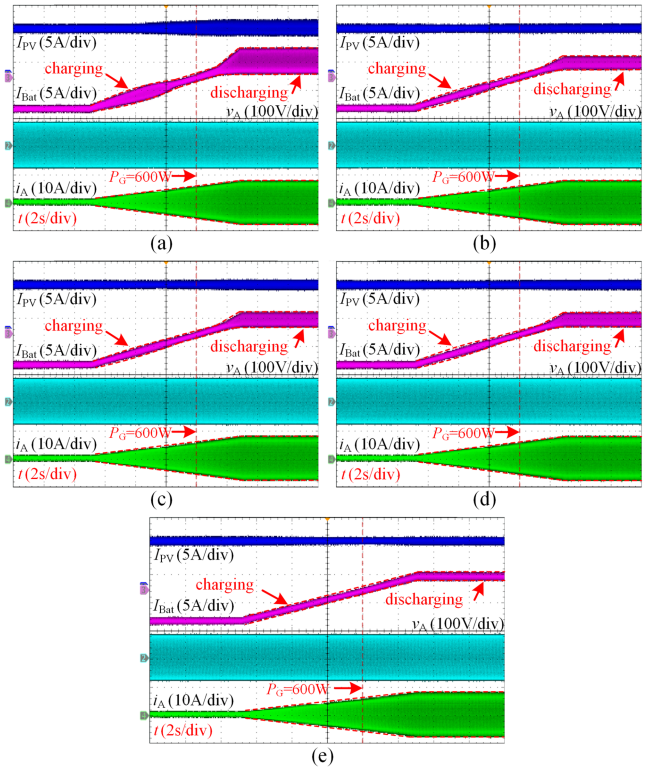

Fig. 22. Dynamic-state waveforms of I_{Bat}, I_{PV}, v_A, i_A when P_G gradually increases from 0 W to 1 kW for the multiport mode. (a) $u_0 = 0$. (b) $u_0 =$ DPWMMAX. (c) $u_0 =$ DPWM-MIN. (d) $u_0 =$ DPWM-MID. (e) $u_0 =$ proposed optimal ZSC injection method.

and smooth dynamic-state performance is also achieved for the proposed optimal ZSC injection method.

To verify the operational mode switching of improved TPTL-MPC and the current ripples of the dc ports when the PV power changes, dynamic-state experimental waveforms when the PV power jumps between 300 and 600 W are shown in Fig. 21. The grid power remains constant at 450 W, and the PV consistently operates at its maximum power point whether the maximum power point of PV varies. When the PV power (600 W) is greater than the grid power (450 W), the battery absorbs the remaining power (about −150 W). When the PV power (300 W) is less than the grid power (450 W), the battery supplements the required power deficit (about 150 W). Moreover, it can be seen that the battery can quickly supply or absorb power, and the grid current remains stable, when the PV power jumps. According to the comparison of experimental results in Fig. 21(a) and (b), the current ripples of PV and battery can also be significantly reduced by the proposed optimal ZSC injection method under the PV power variation.

The dynamic-state waveforms of I_{Bat}, I_{PV}, v_A, i_A are given in Fig. 22 when P_G gradually increases from 0 W to 1 kW for the multiport mode. When the grid power is zero, all the energy of PV is transmitted to the battery through the buck-boost unit. Then, the charging current of battery is maximum. When the grid power is about 600 W, the battery current is almost zero, not participating in energy transmission, and the current ripple of battery is also relatively small. Therefore, the current ripple of PV gradually increases as the grid power increases. However, the battery current ripple initially increases and subsequently decreases as the grid power increases from 0 to 600 W. And the current ripple of battery gradually increases as the grid power increases from 600 W to 1 kW. Clearly, the battery is in a charging state when the grid power is below 600 W, and it discharges when the grid power exceeds 600 W. By comparing experimental results with different ZSC, in the multiport mode, it can be seen that the proposed optimal ZSC injection method can effectively reduce low-frequency current ripples of the PV and battery throughout the full load range.

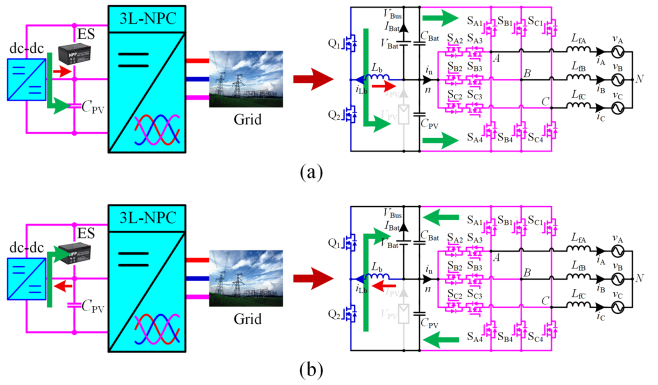

Fig. 23. Operating states of improved TPTL-MPC when the battery and grid are available. (a) Battery to grid mode. (b) Grid to battery mode.

C. Bidirectional Experiment of the Battery and Grid

Operating states of improved TPTL-MPC when the battery and grid are available are shown in Fig. 23. When the T-type NPC unit is in inverter state (the battery to grid mode) or rectifier state (the grid to battery mode), the bidirectional buck-boost unit is

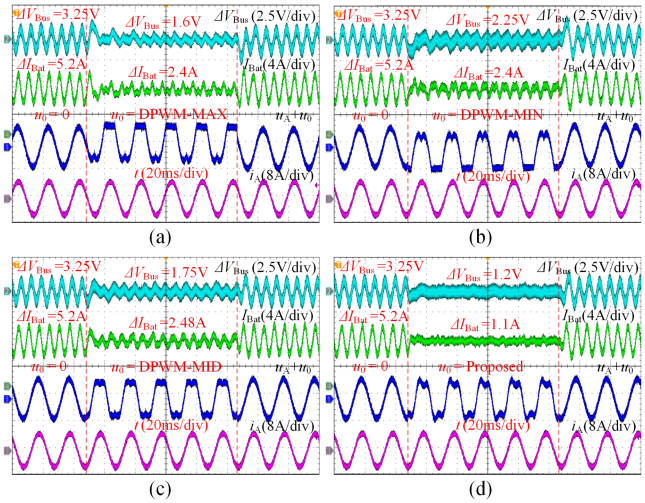

Fig. 24. Dynamic-state waveforms of $\Delta V_{\rm Bus}$, $I_{\rm Bat}$, u_A+u_0, i_A when the ZSC u_0 is switched for the battery to grid mode. (a) u_0 = DPWM-MAX. (b) u_0 = DPWM-MIN. (c) u_0 = DPWM-MID. (d) u_0 = proposed optimal ZSC injection method.

used to stabilize bus voltage. The above-mentioned experimental results are obtained under the multiport mode. In order to verify the bidirectional power flow capability of the battery and grid ports, the bidirectional experimental results are illustrated in Figs. 24 and 25. The dynamic-state waveforms of $\Delta V_{\rm Bus}$, $I_{\rm Bat}$, u_A+u_0, i_A are shown in Fig. 24 when the ZSC u_0 is switched for the battery-to-grid mode. In multiport mode, the low-frequency ripples are mainly reflected in the current of inductor, PV, and battery. In the battery-to-grid mode, and in the grid-to-battery mode, the low-frequency ripples are mainly reflected in the battery current and the bus voltage. It can be seen from Fig. 24 that the low-frequency ripple of the bus voltage and the battery current can be effectively suppressed by adopting the proposed optimal ZSC injection method.

The dynamic-state waveforms of $V_{\rm Bus}$, $I_{\rm Bat}$, v_A, i_A in different ZSC are shown in Fig. 25 when the grid is switched between inverter state and rectifier state. The $V_{\rm Bus}$ is controlled at 180 V. The experimental results show that both the grid port and battery port can operate bidirectionally, and the switching is smooth, allowing for rapid attainment of new reference value. On the other hand, the proposed optimal ZSC injection method can effectively and significantly reduce battery current ripple and bus voltage ripple (the bus voltage ripple is the voltage ripple of PV port). And it is effective in both battery-to-grid mode and grid-to-battery mode, which is consistent with theoretical analysis.

D. Inductor Current Ripple Ratio, Efficiency, and THD Results

To visually demonstrate the suppression effect of low-frequency ripples, the relationship between grid power P_G and inductor current ripple ratio for different ZSC injection methods is shown in Fig. 26(a). It can be seen that the inductor current ripple by using the proposed optimal ZSC injection method is significantly reduced. As P_G increases, the inductor current decreases, while the high-frequency ripple of inductor current remains largely unchanged, and the low-frequency ripple increases. Therefore, the enhancement of P_G has led to the increase of the inductor current ripple ratio. The inductor current ripple ratio $r_{\rm Lb}$ for the proposed optimal ZSC injection method can be calculated as follows:

$$r_{\rm Lb}=\frac{\Delta I_{\rm Lb\_HF}}{i_{\rm Lb}}=\frac{b}{a-P_G},\ (a=I_{\rm PV}(V_{\rm Bat}+V_{\rm PV}),$$
$$b=\frac{V_{\rm Bat}^2V_{\rm PV}}{L_bf_b(V_{\rm Bat}+V_{\rm PV})}). \tag{30}$$

In multiport mode, the PV operates in MPPT mode, where the power of PV remains constant. According to (30), the coefficients a and b are constant values under stable state. For the experimental parameters in Table IV, the coefficients a and b are equal to 1400 and 157.99 (unit: W). And the inductor current ripple ratio $r_{\rm Lb}$ can be calculated as follows:

$$r_{\rm Lb}=\frac{\Delta I_{\rm Lb\_HF}}{i_{\rm Lb}}=\frac{b}{a-P_G}=\frac{157.99}{1400-P_G}. \tag{31}$$

For the proposed optimal ZSC injection method, as shown in Fig. 26(a), the experimental result (red line) is consistent with the theoretical result (green line). It should be noted that the $(a-P_G)$ in (31) decreases gradually with the increase in grid power, and the power loss of T-type NPC unit is also gradually increasing. Therefore, the error between theoretical and experimental results increases with the increase in P_G.

Fig. 26(b) illustrates efficiency results of the improved TPTL-MPC in multiport mode. Moreover, compared with noninjected ZSC, the proposed optimal ZSC injection method can further improve efficiency. In addition, when the P_G is below 600 W, the PV supplies power to both the battery and grid. When the P_G exceeds 600 W, the PV and battery supply power to grid. The peak efficiency of the improved TPTL-MPC is 96.5% by using proposed ZSC injection method in multiport mode. The maximum ZSC injection method has the minimum midpoint current and the lowest efficiency. Conversely, the minimum ZSC injection method has the maximum midpoint current and the highest efficiency. And because the amount of energy that can be conducted through the midpoint is inherently limited, the efficiency differences in various ZSC injection methods are relatively small.

Fig. 26(c) shows THD results of the grid current in multiport mode. As the grid-connected power increases, the THD of the grid current gradually decreases. Moreover, it is evident that the THDs under maximum ZSC and minimum ZSC injection methods are relatively high. The phenomenon occurs due to the inactivity of switching devices under some operating states. In contrast, the differences in THD among the other three methods are comparatively small.

Consequently, Table III provides qualitative comparison of the structural features and operational characteristics of the various MPCs, while Fig. 26 presents quantitative comparison of the several ZSC methods for improved TPTL-MPC. The proposed optimal ZSC injection method has the minimum inductor current ripple ratio and takes into account the better performance in terms of both efficiency and THD.

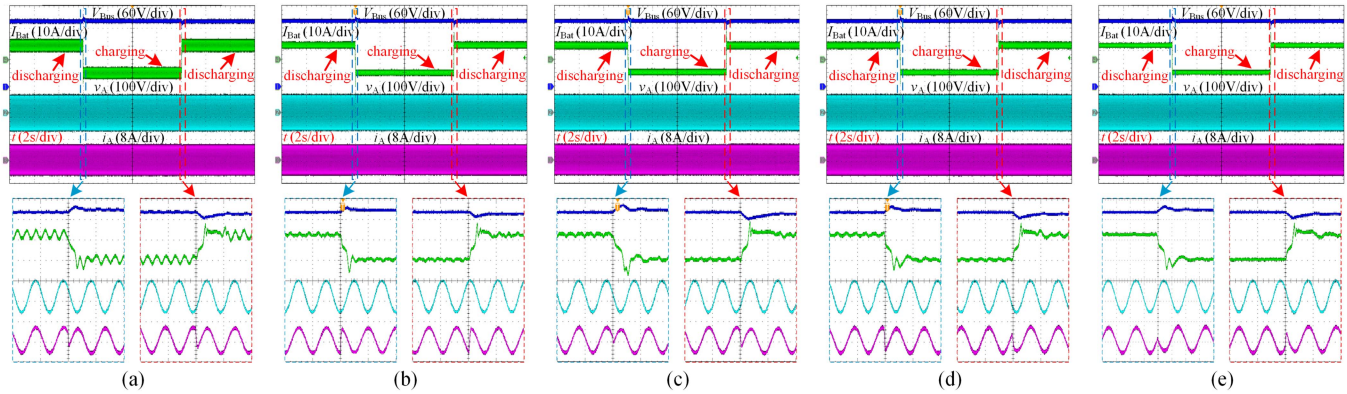

Fig. 25. Dynamic-state waveforms of $V_{\rm Bus}, I_{\rm Bat}, v_A, i_A$ when the grid is switched between inverter state and rectifier state. (a) $u_0 = 0$. (b) $u_0 =$ DPWM-MAX. (c) $u_0 =$ DPWM-MIN. (d) $u_0 =$ DPWM-MID. (e) $u_0 =$ proposed optimal ZSC injection method.

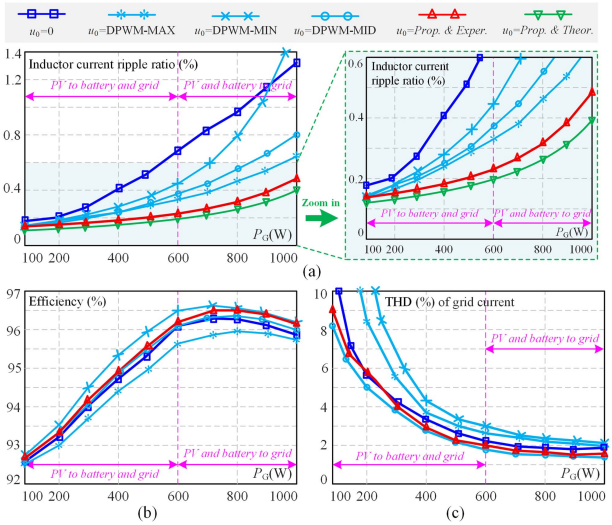

Fig. 26. Experimental results of inductor current ripple ratio, efficiency, and THD under several ZSC injection methods. (a) Relationship between inductor current ripple ratio and grid power. (b) Efficiency results of improved TPTL-MPC. (c) THD of grid current.

VI. Conclusion

The improved TPTL-MPC is presented for the PV, battery and grid hybrid systems, which has reduced power conversion stage and voltage requirements of the PV and battery ports. The DVR-SPWM and its digital implementation is proposed in this article, with lower THD of grid current. Based on the improved TPTL-MPC and DVR-SPWM, the optimal ZSC injection method is proposed, which can eliminate voltage and current low-frequency ripples of the inductor, PV and battery. Compared with other ZSC injection methods, the proposed optimal ZSC injection method can reduce low-frequency voltage and current ripples under different operational modes, the dc port voltage, the displacement angle, and the grid power. The effectiveness and correctness of an optimal ZSC injection method with reduced low-frequency voltage and current ripples for the improved TPTL-MPC are verified by the experiment results and performance comparison with noninjected ZSC and other ZSC injection method.

References

[1] Y. Yang, Y. Qin, S.-C. Tan, and S. Y. R. Hui, "Efficient improvement of photovoltaic-battery systems in standalone DC microgrids using a local hierarchical control for the battery system," *IEEE Trans. Power Electron.*, vol. 34, no. 11, pp. 10796–10807, Nov. 2019.

[2] A. K. Bhattacharjee, N. Kutkut, and I. Batarseh, "Review of multiport converters for solar and energy storage integration," *IEEE Trans. Power Electron.*, vol. 34, no. 2, pp. 1431–1445, Feb. 2019.

[3] Z. Wang, Q. Luo, Y. Wei, D. Mou, X. Lu, and P. Sun, "Topology analysis and review of three-port DC-DC converters," *IEEE Trans. Power Electron.*, vol. 35, no. 11, pp. 11783–11800, Nov. 2020.

[4] Y. Karimi, H. Oraee, M. S. Golsorkhi, and J. M. Guerrero, "Decentralized method for load sharing and power management in a PV/battery hybrid source islanded microgrid," *IEEE Trans. Power Electron.*, vol. 32, no. 5, pp. 3525–3535, May 2017.

[5] Q. Tian, G. Zhou, L. Wang, Q. Bi, and M. Leng, "Symmetric bipolar output full-bridge four-port converter with phase-shift modulated buck-boost voltage balancer," *IEEE Trans. Ind. Electron.*, vol. 69, no. 8, pp. 8040–8054, Aug. 2022.

[6] K. Rahbar, C. C. Chai, and R. Zhang, "Energy cooperation optimization in microgrids with renewable energy integration," *IEEE Trans. Smart Grid*, vol. 9, no. 2, pp. 1482–1493, Mar. 2018.

[7] Z. Yi, W. Dong, and A. H. Etemadi, "A unified control and power management scheme for PV-battery-based hybrid microgrids for both grid-connected and islanded modes," *IEEE Trans. Smart Grid*, vol. 9, no. 6, pp. 5975–5985, Nov. 2018.

[8] H. Han, X. Hou, J. Yang, J. Wu, M. Su, and J. M. Guerrero, "Review of power sharing control strategies for islanding operation of ac microgrids," *IEEE Trans. Smart Grid*, vol. 7, no. 1, pp. 200–215, Jan. 2016.

[9] Y. Shan, J. Hu, M. Liu, J. Zhu, and J. M. Guerrero, "Model predictive voltage and power control of islanded PV-battery microgrids with washout filter-based power sharing strategy," *IEEE Trans. Power Electron.*, vol. 35, no. 2, pp. 1227–1238, Feb. 2020.

[10] S. Devassy and B. Singh, "Performance analysis of solar PV array and battery integrated unified power quality conditioner for microgrid systems," *IEEE Trans. Ind. Electron.*, vol. 68, no. 5, pp. 4027–4035, May 2021.

[11] V. Narayanan, S. Kewat, and B. Singh, "Control and implementation of a multifunctional solar PV-BES-DEGs based microgrid," *IEEE Trans. Ind. Electron.*, vol. 68, no. 9, pp. 8241–8252, Sep. 2021.

[12] Y. Singh, B. Singh, and S. Mishra, "Multifunctional control for PV integrated battery energy storage system with improved power quality," *IEEE Trans. Ind. Appl.*, vol. 56, no. 6, pp. 6835–6845, Nov./Dec. 2020.

[13] N. Hou and Y. W. Li, "Overview and comparison of modulation and control strategies for a nonresonant single-phase dual-active-bridge DC-DC converter," *IEEE Trans. Power Electron.*, vol. 35, no. 3, pp. 3148–3172, Mar. 2020.

[14] F. Nejabatkhah and Y. W. Li, "Overview of power management strategies of hybrid AC/DC microgrid," *IEEE Trans. Power Electron.*, vol. 30, no. 12, pp. 7072–7089, Dec. 2015.

[15] H. R. Teymour, D. Sutanto, K. M. Muttaqi, and P. Ciufo, "Solar PV and battery storage integration using a new configuration of a three-level NPC inverter with advanced control strategy," *IEEE Trans. Energy Convers.*, vol. 29, no. 2, pp. 354–365, Jun. 2014.

[16] Z. Huang, D. Zhou, L. Wang, Z. Shen, and Y. Li, "A review of single-stage multiport inverters for multisource applications," *IEEE Trans. Power Electron.*, vol. 38, no. 5, pp. 6566–6584, May 2023.
[17] Q. Zhang and K. Sun, "A flexible power control for PV-battery hybrid system using cascaded H-bridge converters," *IEEE J. Emerg. Sel. Top. Power Electron.*, vol. 7, no. 4, pp. 2184–2195, Dec. 2019.
[18] S. Neira, J. Pereda, and F. Rojas, "Three-port full-bridge bidirectional converter for hybrid DC/DC/AC systems," *IEEE Trans. Power Electron.*, vol. 35, no. 12, pp. 13077–13084, Dec. 2020.
[19] J. Wang, K. Sun, D. Zhou, and Y. Li, "Virtual SVPWM-based flexible power control for dual-DC-port DC-AC converters in PV-battery hybrid systems," *IEEE Trans. Power Electron.*, vol. 36, no. 10, pp. 11431–11443, Oct. 2021.
[20] C. Xue, J. Wang, and Y. Li, "Model predictive control for grid-tied multi-port system with integrated PV and battery storage," *IEEE Trans. Smart Grid*, vol. 13, no. 6, pp. 11020–11033, Nov. 2022.
[21] L. Liu, D. Zhou, J. Zou, and W. Wang, "Decoupled modeling and wide-range power distribution strategy for the multisource inverter in microgrids," *IEEE Trans. Smart Grid*, vol. 13, no. 6, pp. 11020–11033, Nov. 2022.
[22] Q. Yan, H. Chen, T. Zhao, X. Yuan, L. Zhang, and R. Zhao, "A carrier-based discontinuous space-vector PWM for common-mode voltage reduction in dual-input three-level T-type inverters with unbalanced neutral-point voltages," *IEEE Trans. Power Electron.*, vol. 38, no. 10, pp. 12078–12090, Oct. 2023.
[23] J. Wang, K. Sun, C. Xue, T. Liu, and Y. Li, "Multi-port DC-AC converter with differential power processing DC-DC converter and flexible power control for battery ESS integrated PV systems," *IEEE Trans. Ind. Electron.*, vol. 69, no. 5, pp. 4879–4889, May 2022.
[24] N. Kim and B. Parkhideh, "PV-Battery series inverter architecture: A solar inverter for seamless battery integration with partial-power DC-DC optimizer," *IEEE Trans. Energy Convers.*, vol. 34, no. 1, pp. 478–485, Mar. 2019.
[25] A. A. Saafan, V. Khadkikar, A. Edpuganti, M. S. E. Moursi, and H. H. Zeineldin, "A novel nonisolated four-port converter for flexible DC micro grid operation," *IEEE Trans. Ind. Electron.*, vol. 71, no. 2, pp. 1653–1664, Feb. 2024.
[26] Z. Lin et al., "An integrated flying capacitor three-level DC/DC converter with mismatch power processing capability," *IEEE J. Emerg. Sel. Top. Power Electron.*, vol. 12, no. 1, pp. 765–778, Feb. 2024.
[27] B. Liu et al., "Input current ripple and grid current harmonics restraint approach for single-phase inverter under battery input condition in residential photovoltaic/battery systems," *IEEE Trans. Sustain. Energy*, vol. 9, no. 4, pp. 1957–1968, Oct. 2018.
[28] K. Zhou and D. Wang, "Relationship between space-vector modulation and three-phase carrier-based PWM: A comprehensive analysis," *IEEE Trans. Ind. Electron.*, vol. 49, no. 1, pp. 186–196, Feb. 2002.
[29] J. Pou, J. Zaragoza, S. Ceballos, M. Saeedifard, and D. Boroyevich, "A carrier-based PWM strategy with zero-sequence voltage injection for a three-level neutral-point-clamped converter," *IEEE Trans. Power Electron.*, vol. 27, no. 2, pp. 642–651, Feb. 2012.
[30] R. Maheshwari, S. Busquets-Monge, and J. Nicolas-Apruzzese, "A novel approach to generate effective carrier-based pulsewidth modulation strategies for diode-clamped multilevel DC-AC converters," *IEEE Trans. Ind. Electron.*, vol. 63, no. 11, pp. 7243–7252, Nov. 2016.
[31] Q. Tian, G. Zhou, H. Li, Y. Yang, and D. Zhou, "Symmetrical bipolar output isolated four-port converters based on center-tapped winding for bipolar DC bus applications," *IEEE Trans. Power Electron.*, vol. 37, no. 2, pp. 2338–2351, Feb. 2022.

Nengmou Xu (Student Member, IEEE) received the B.S. degree in electrical engineering and automation from Qinghai University, Xining, China, in 2019. He is currently working toward the Ph.D. degree in electrical engineering with Southwest Jiaotong University, Chengdu, China.

His research interests include multilevel inverter topologies, multiport power converter, and its control strategies for renewable energy and energy storage systems.

Guohua Zhou (Senior Member, IEEE) received the B.S. degree in electronic and information engineering and the M.S. and Ph.D. degrees in electrical engineering from Southwest Jiaotong University, Chengdu, China, in 2005, 2008, and 2011, respectively.

From March 2010 to September 2010, he was a Research Assistant with the Department of Electronic and Information Engineering, Hong Kong Polytechnic University, Kowloon, Hong Kong. From October 2010 to March 2011, he was a Visiting Scholar (also a Joint Ph.D. student) with the Center for Power Electronics Systems, Virginia Polytechnic Institute and State University, Blacksburg, VA, USA. He is currently a Professor with the School of Electrical Engineering, Southwest Jiaotong University. His current research interests include modulation and control techniques of power electronics systems, modeling and stability analysis of switching power converters, and renewable energy applications of power electronics.

Dr. Zhou was the recipient of the National Excellent Doctoral Dissertation of China in 2014. He was elected as a Fellow of the Institution of Engineering and Technology in 2018. He is currently an Associate Editor of *CPSS Transactions on Power Electronics and Applications*.

Yingjie He was born in Sichuan Province, China, in 2001. He received the B.S. degree in microelectronic science and engineering from Chengdu Technological University, Chengdu, China, in 2023. He is currently working toward the M.S. degree in electrical engineering with Southwest Jiaotong University, Chengdu, China. His research interests include high-efficiency dc–dc converter topologies and control strategies, as well as modulation and control strategies for pulse width modulation rectifiers.

Qingxin Tian (Member, IEEE) received the B.S. degree in electronic and information engineering and the Ph.D. degree in electrical engineering from Southwest Jiaotong University, Chengdu, China, in 2017 and 2022, respectively.

From 2021 to 2022, he was a Visiting Ph.D. Student with the Department of Energy Technology, Aalborg University, Aalborg, Denmark. From July 2022 to July 2024, he was working as a Postdoctoral Research Fellow with Zhejiang University, Hangzhou, China. He is currently an Associate Researcher with Southwest Jiaotong University. His research interests include renewable energy system, topology and control of multiport power converters, bipolar power conversion technology, and modeling and control techniques of power converters.

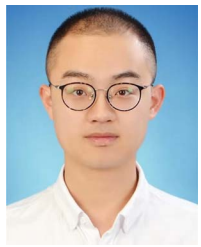

Qiang Bi was born in Liaoning Province, China, in 1996. He received the B.S. degree in electrical engineering and automation from Northeast Petroleum University, Daqing, China, in 2018, and the Ph.D. degree in electrical engineering from Southwest Jiaotong University, Chengdu, China, in 2023.

Since 2023, he has been with the Department of Electrical Engineering, Tsinghua University (THU), as a Postdoctoral Research Fellow and an Assistant Researcher. His research interests include power electronics, control of renewable energy systems, fault diagnosis of PV, and power quality of distribution network.

Wenjun Zeng received the B.S. degree in automation from Nanchang Hangkong University, Nanchang, China, in 2020, and the M.S. degree in electrical engineering from the School of Electrical Engineering, Nanchang Institute of Technology, Nanchang, China, in 2023. He is currently working toward the Ph.D. degree in electrical engineering with Southwest Jiaotong University, Chengdu, China.

His current research interests include multilevel inverters and modulation strategy.